Fluid Dynamics of Unsteady Cavity Flow

W. A. Engblom and D. Goldstein
Institute for Advanced Technology
The University of Texas at Austin

November 1996

IAT.R 0121

IAT Institute for Advanced Technology
The University of Texas at Austin

The views, opinions, and/or findings contained in this report are those of the author(s) and should not be construed as an official Department of the Army position, policy, or decision, unless so designated by other documentation.

REPORT DOCUMENTATION PAGE

Form Approved
OMB NO. 0704-0188

1. AGENCY USE ONLY (Leave blank)	2. REPORT DATE	3. REPORT TYPE AND DATES COVERED
	November 1996	Technical Report

4. TITLE AND SUBTITLE

Fluid Dynamics of Unsteady Cavity Flow

5. FUNDING NUMBERS

Contract # DAAA21-93-C-0101

6. AUTHOR(S)

W. A. Engblom and D. Goldstein

7. PERFORMING ORGANIZATION NAME(S) AND ADDRESS(ES)

Institute for Advanced Technology
The University of Texas at Austin
4030-2 W. Braker Lane, #200
Austin, TX 78759

8. PERFORMING ORGANIZATION REPORT NUMBER

IAT.R 0121

9. SPONSORING / MONITORING AGENCY NAME(S) AND ADDRESS(ES)

U.S. Army Research Laboratory
ATTN: AMSRL-WT-T
Aberdeen Proving Ground, MD 21005-5066

10. SPONSORING / MONITORING AGENCY REPORT NUMBER

11. SUPPLEMENTARY NOTES

The view, opinions and/or findings contained in this report are those of the author(s) and should not be considered as an official Department of the Army position, policy, or decision, unless so designated by other documentation.

12a. DISTRIBUTION / AVAILABILITY STATEMENT

Approved for public release; distribution unlimited.

12b. DISTRIBUTION CODE

A

13. ABSTRACT *(Maximum 200 words)*

Unsteady, hypersonic flow over the nose of a blunt body with a forward-facing cavity is studied. A parameter study is conducted using a commercial finite-volume computer code to study the mechanisms of resonance. Numerical simulation results are often directly compared to recent experiments. Resonant pressure oscillations within the cavity occur for relatively shallow cavities provided freestream noise is present. However, deeper cavities self-sustain strong resonance. A spring-mass-damper model is described which emulates noise-driven, relatively shallow cavity acoustic behavior.

14. SUBJECT TERMS

Acoustic, Cavity, Hypersonic, Numerical

15. NUMBER OF PAGES

60

16. PRICE CODE

17. SECURITY CLASSIFICATION OF REPORT	18. SECURITY CLASSIFICATION OF THIS PAGE	19. SECURITY CLASSIFICATION OF ABSTRACT	20. LIMITATION OF ABSTRACT
Unclassified	Unclassified	Unclassified	UL

DISCLAIMER NOTICE

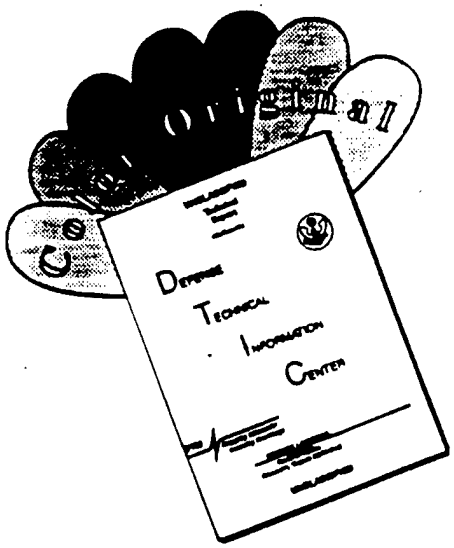

THIS DOCUMENT IS BEST QUALITY AVAILABLE. THE COPY FURNISHED TO DTIC CONTAINED A SIGNIFICANT NUMBER OF COLOR PAGES WHICH DO NOT REPRODUCE LEGIBLY ON BLACK AND WHITE MICROFICHE.

Table of Contents

List of Figures

1.1 Motivation

Hypersonic vehicles are designed to withstand severe heat loads. Such vehicles include hypervelocity projectiles, interceptor missiles, re-entry vehicles, and hypersonic aircraft. Maximum heating and, hence, the potential for material ablation, is typically most critical at the nose tip.

Of particular interest herein are hypervelocity projectiles. Such projectiles can have large penetration depths into armor due to their very high kinetic energy at impact [Refs. 1,2] and consequently the U.S. Army is interested in their development. Between 1.5 km/sec and 2 km/sec at sea level the projectile nose-tip can withstand the aerodynamic thermal environment provided a high melting-point material such as tungsten is used. However, in the flight regime 2-4 km/sec, the projectile nose-tip experiences severe heat rates and shape change due to ablation can occur. The shape change can produce unacceptable perturbations in the aerodynamics and the flight path and also reduce penetration characteristics. As an example of the severity of the heating, the stagnation temperature at standard sea level conditions and a velocity of 3.1 km/s (Mach 8.9) corresponds to the melting point of tungsten (3680 K). Consequently, to extend the flight regime above 2 km/s there is a need to develop active or passive techniques to reduce tip heating rates.

There has been speculation that introducing an axial cavity in the blunt nose region of a hypersonic vehicle (Fig. 1) may reduce surface heating during flight. This speculation was based on two observations. First, there is substantial experimental evidence that stagnation point heat transfer is reduced for certain nose-cavity configurations. Specifically, the heat transfer rate at the cavity base is low compared to standard nose-tip stagnation-point heat rates. Second, there is recent experimental evidence that the heat transfer along the outer surface, near the cavity lip, is significantly reduced for certain nose-cavity configurations compared to spherical nose-tips. Finally, there is abundant experimental evidence that nose-cavity flow resonates strongly at a discrete frequency. It was thought that perhaps this resonance affects the boundary layer over the nose/cavity in such a way so as to change the mean heat transfer. Consequently, the concept of a forward-facing cavity for overall nose-tip surface heat reduction is at least plausible.

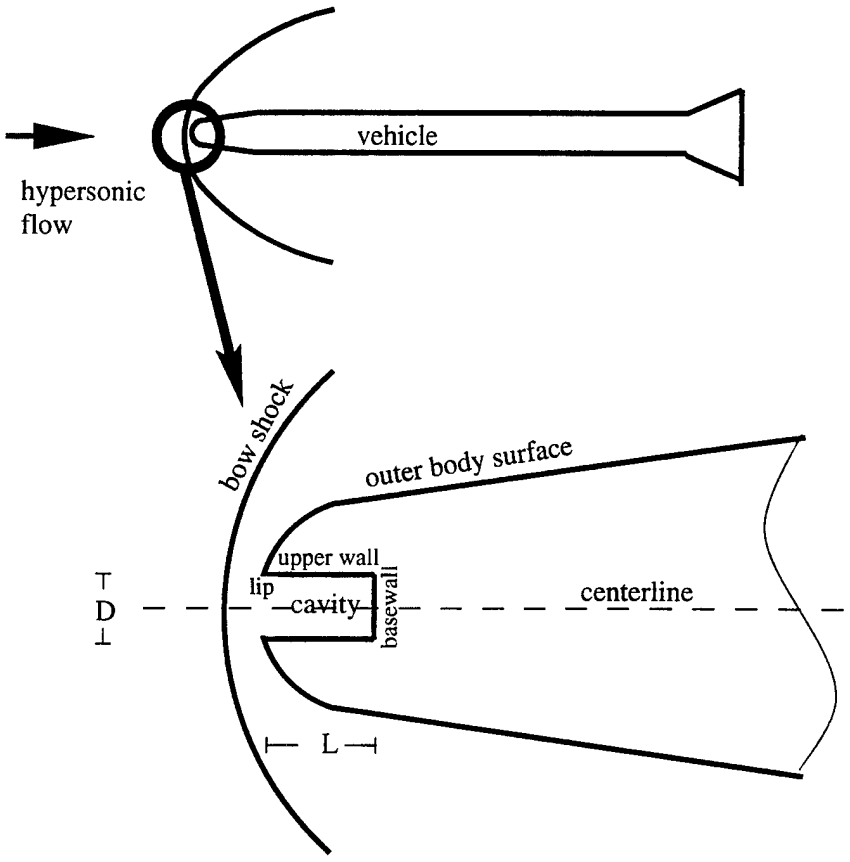

Fig. 1 : Schematic of axial cavity in the nose region of a hypersonic vehicle

1.2 Objectives

The objective of this report is to lay out the details of an analysis of the fluid dynamics of unsteady cavity flow. The bulk of our other results have appeared elsewhere. An initial comparison between experiment and numerical results appeared in Engblom et. al. [Ref. 3]. A discussion of the numerical simulation results for oscillating cavity flow appeared in Engblom et. al. [Ref. 4] while a presentation of the nose tip heating results appeared in Engblom and Goldstein [Ref. 5]. An overall compendium of the work is found in Engbom's dissertation [Ref. 6] including a review of the relevant literature and the details of the commercial Computational Fluid Dynamics (CFD) package used.

The material herein consists mostly of material from chapter 5 of Engblom's dissertation. It begins with a discussion of the origin of the primary "organ-pipe" frequency found in cavity oscillations and then covers the mechanisms of cavity resonance. The resonance is very similar to the motion of a damped harmonic oscillator. This observation leads to the development of a spring-mass-damper (SMD) model of shallow cavity oscillation. This SMD model is then compared to the results of the full CFD simulations. Finally, in deeper cavities it is found that self-sustained oscillations occur in the CFD and this phenomenon is discussed in the final section.

2 Primary 'Organ-Pipe' Frequency

Oscillating pressure levels within a cavity are a dominant *experimental* flow feature in forward-facing cavity configurations. Resonant frequencies are obtained by spectral analysis of the fluctuating pressure measurements made in the cavity. Most of the energy of the oscillations is contained in a primary mode frequency. The pressure oscillations within the cavity are found to be essentially axial (1-D) based on two-point spatio-temporal correlations [Refs. 1,2,3,7,8]. The rms amplitude of the oscillations increases along the cavity walls from the cavity mouth to a maximum at the cavity basewall [Ref. 9].

Primary frequencies (f_1) can be estimated *a priori* from a simple linear relation derived from the 1-d wave equation in classic organ-pipe theory by considering only the characteristic wavelength (λ) and the speed of sound (c_o) inside the cavity:

$$f_1 = \frac{c_o}{\lambda} \tag{1}$$

Time accurate flow animations for modestly large diameter cavities (described later) indicate that pressure waves travel between the bow shock and the base of the cavity. These pressure waves are reflected off the base wall and inverted off the bow shock. Consequently, an appropriate length λ is four times the distance between the mean bow shock location and the cavity base along the centerline (L^*). Numerical steady flowfield solutions indicate that the flow is virtually stagnant inside the cavity. Consequently, the speed of sound c_o can be estimated assuming the gas temperature inside the cavity is approximately the stagnation temperature (T_o) of the flow. Thus,

$$f_1 = \frac{\sqrt{\gamma R T_o}}{4L^*} \tag{2}$$

As seen in Fig. 2, this equation clearly provides good agreement with primary frequencies derived from various experimental runs and time-accurate numerical simulations. The shock standoff distances required for the frequency calculations are obtained from either schlieren photographs or steady flow CFD solutions. Note that the straight line with slope of 1 represents perfect agreement between the theoretical (Eqn. 2) and measured frequencies. The agreement is generally best for the deepest cavities (i.e., lower frequencies).

3 Mechanisms of Resonance

In order to study the mechanisms of resonance we first compare numerical simulation results to experimental results for the same body configuration and freestream conditions at Mach 5 (Engblom (Ref 6), Section 3.3). The numerical input noise is adapted from a broad spectrum 'white noise' data set obtained from pitot

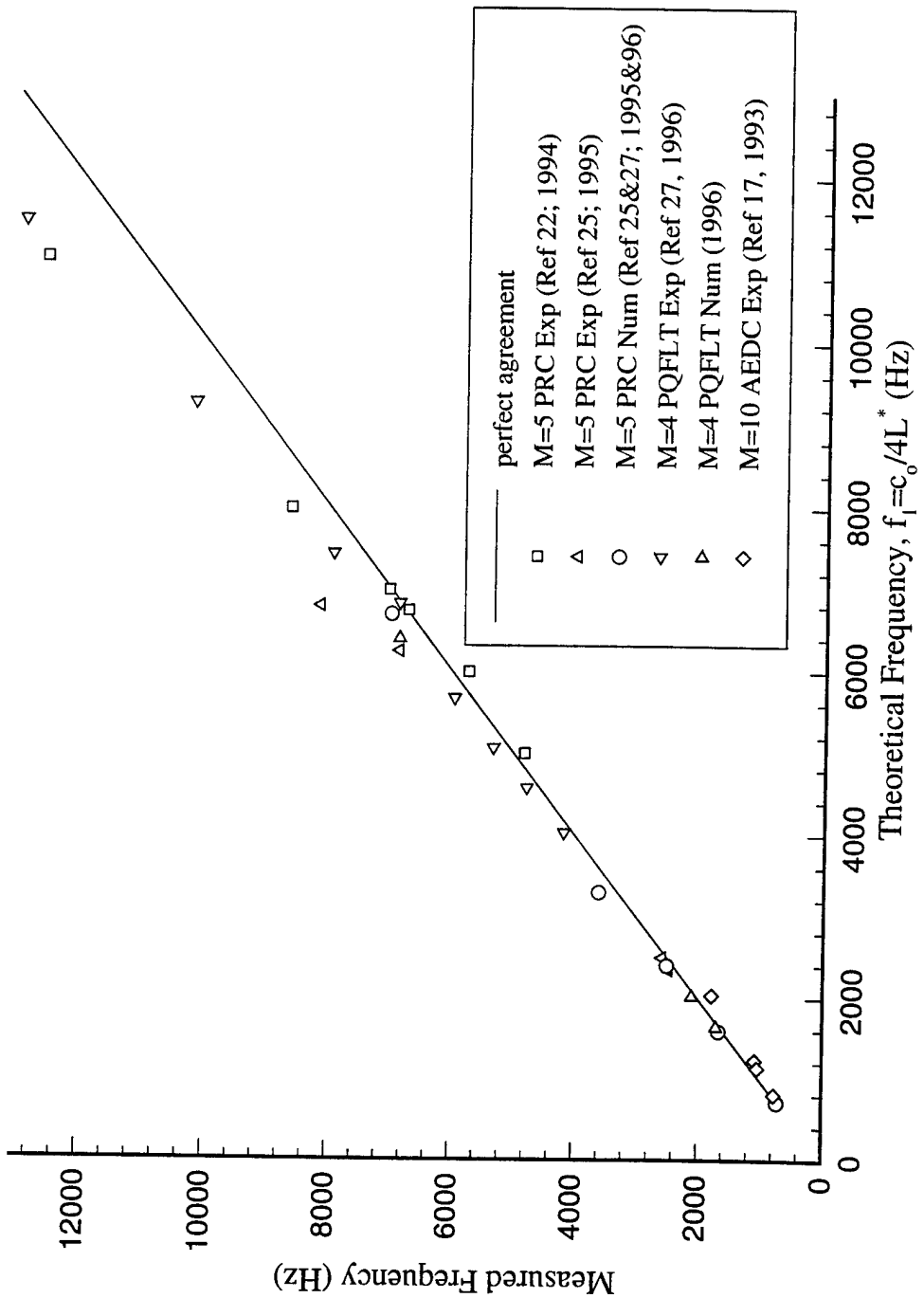

Fig. 2 : Cavity frequency response

stagnation pressure (Pt_2) measurements on a blunt body in the University of Texas at Austin, Pickle Research Center (UTA, PRC) Mach 5 blowdown facility (Ref. 6, Section 3.3). This data set is re-scaled to provide a numerical inflow noise history and retain the same rms variation of approximately ±1.15%. Numerical simulations involve more than 50 oscillations at the primary frequency. The rms of base pressure fluctuations is estimated from the base pressure history after the oscillations are 'stable' (i.e., after the initial 3-10 cycles for most cases). Another set of numerical simulations without inflow noise (steady inflow conditions) is also computed.

Input perturbations typically result in large stagnation pressure oscillations at the base of the cavity. The amplification (G) is defined as the ratio of the output (centerline base pressure) rms amplitude to the input (freestream) rms amplitude:

$$G = \frac{P_{base_{rms}}}{P_{\infty_{rms}}} \tag{3}$$

For example, if a cavity driven with a perturbation input rms of ±1.15% P_∞ and ±1.15% ρ_∞ produces an output rms of ±22.3% P_{base}, this results in an amplification of 20.

The numerical results (i.e., portions of the base pressure histories) for various cavity depths at Mach 5 are shown in Fig. 3. Based on power spectrum analysis, most of the oscillation energy is contained within a small band near f_1. Note, the oscillations become 'cleaner' (i.e., more sinusoidal) and stronger with cavity depth. The L/D=3.0 case exhibits 'quasi-static' bow shock motion in which the bow shock remains fixed at the mouth of the cavity during inflow and at an upstream position during outflow and moves abruptly between these two positions. This motion is reflected in the shark-tooth shape of the base pressure trace.

Fig. 4a illustrates how amplification grows with cavity depth in numerical simulations and experiments [Ref. 7] at Mach 5. When freestream noise is present both the numerics and experiments show a gradual increase of oscillation strength with

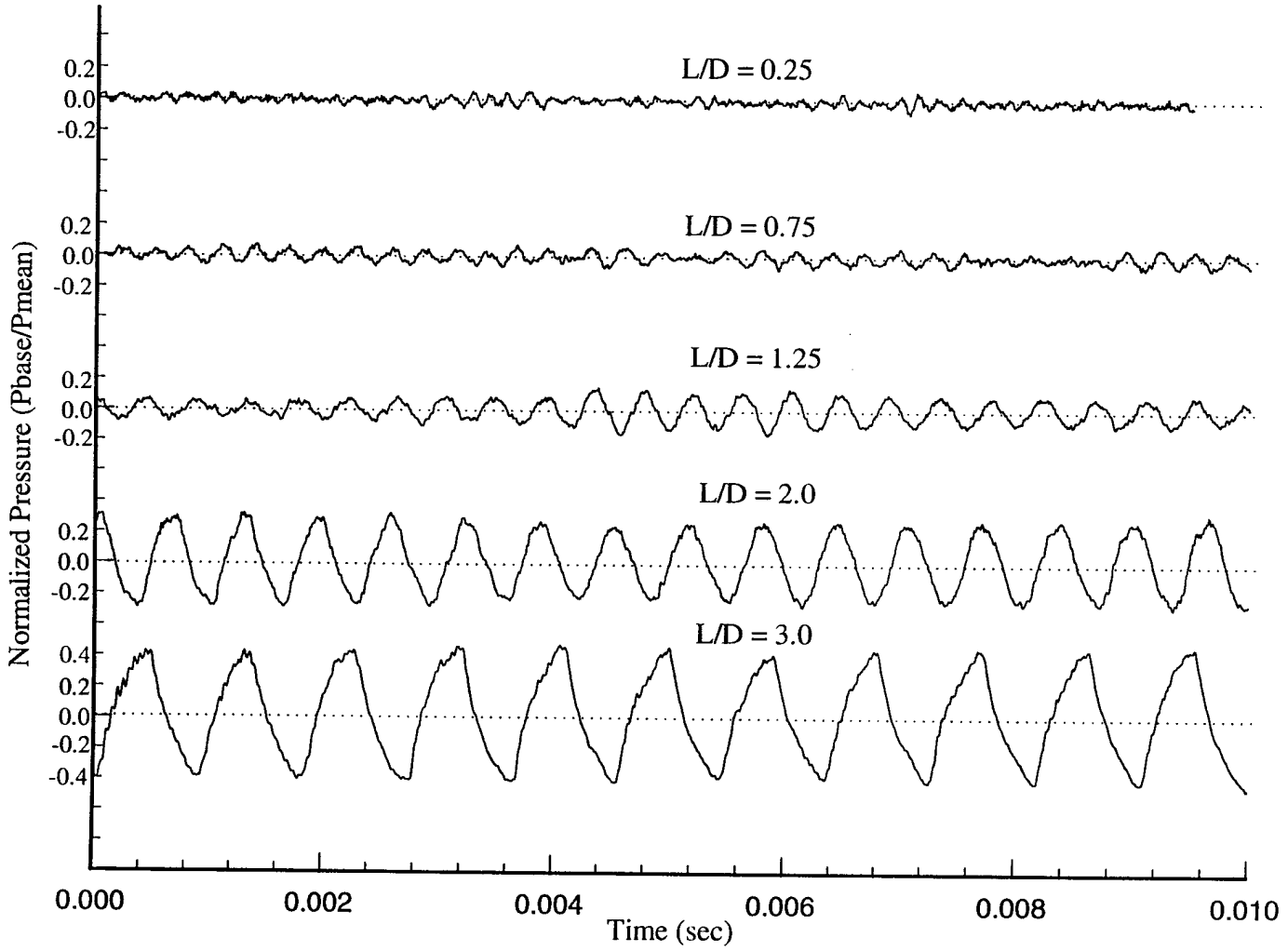

Fig. 3 : Numerical base pressure signals (Mach 5 tunnel conditions)

cavity depth for relatively shallow cavities ($L/D \leq 1.0$). Note that the numerical estimates for shallow cavities involve some statistical uncertainty (approximately ±10%) due to the limited duration of the simulation. Note also that both the numerical and experimental models include a flat basewall. Since the experiments involving medium depth cavities ($0.4 \leq L/D \leq 0.7$) exhibit two modes of resonance [Ref. 2, 3] the rms estimate is somewhat ambiguous and is not included (dotted line). Specifically, in that depth range experiments find that the pressure oscillations switch between a very strong resonance mode and a weak resonance mode at random time intervals. This behavior is also strongly asymmetric and cannot be directly compared to axisymmetric numerical results.

A qualitative change in the curve occurs near L/D=1.0. Fig. 4a shows that the slope of the amplification curve increases dramatically ($L/D > 1.0$) in both the experiments and numerical simulations. However, the numerical model produces a smaller estimate of the oscillations which occur in the experiments. Some of the difference may be due to numerical dissipation of the fast-moving bow shock and strong waves within the cavity; however, a rigorous spatial and temporal sensitivity study of the $L/D = 2.0$ case indicates the numerical solution is converged (see Ref. 6), Section 6.3 for more details on this sensitivity study). Other possible numerical causes of the discrepancy include the axisymmetric and laminar flow assumptions since the experimental flow is not entirely axisymmetric and may include turbulent. The numerical and experimental results are quite sensitive to cavity depth in this regime and it is reasonable to expect that these results are very sensitive to many other parameters.

Fig. 4b illustrates how amplification grows with cavity depth in numerical simulations at Mach 5 with and without freestream noise. Numerical oscillations are only obtained for relatively shallow cavities ($L/D < 1.25$) by introducing freestream noise. These results imply that freestream noise is the mechanism which drives the

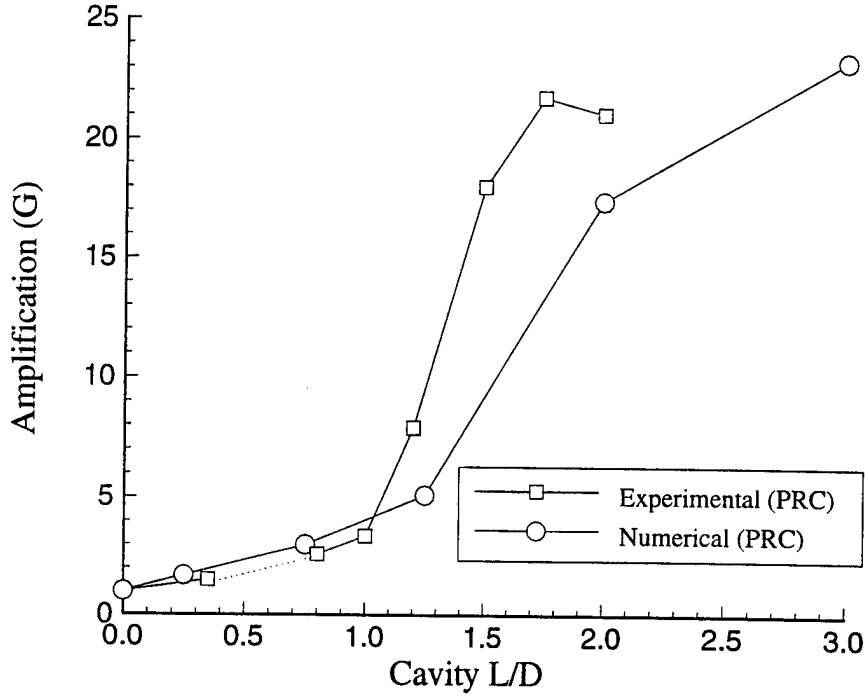

Fig. 4a : Amplification vs. cavity depth (Mach 5 tunnel)

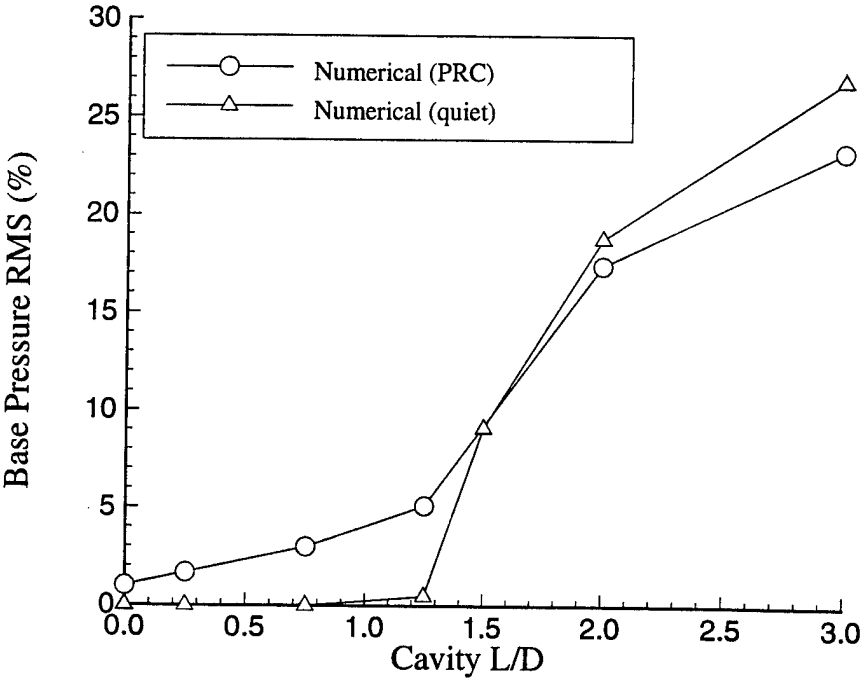

Fig. 4b : Base pressure rms vs. cavity depth (Mach 5)

oscillations for relatively shallow cavities in wind tunnel experiments. The implications of this are discussed in more detail later in this report.

The numerical results in Fig. 4b, however, also indicate that relatively deep cavities are unstable. Specifically, the deeper cavities resonate strongly without freestream noise. This is termed *self-sustained* resonant oscillations. In the deep cavity cases the oscillations are nearly the same strength regardless of whether or not inflow noise is included in the simulation. Potential mechanisms which drive these self-sustaining oscillations are briefly discussed in Section 4.5.

To further validate the claim that freestream noise is the mechanism which drives resonance in relatively shallow cavities, numerical simulation results are compared to the quiet freestream experimental results obtained in the Mach 4 Purdue Quiet Flow Ludwieg Tube (PQFLT) [Ref. 4]. The experimental inflow noise contains a rms variation of only about ±0.048%, based on pitot pressure (Pt_2) variation measurements. The numerical input noise is again adapted from Mach 5 blowdown tunnel measurements except that it is rescaled down by a factor of 24 (from ±1.15%) to obtain the desired rms variation of ±0.048%. Again, more than 50 oscillation cycles are computed for each configuration.

Fig. 5a shows a portion of the experimental base pressure signal for an L/D=1.0 case. The rms of the these fluctuations is approximately ±0.07% ($G \equiv \frac{P_{base,rms}}{P_\infty} = 1.5$). A spectral analysis indicates that the peak level of energy for the full experimental data set is approximately 6300 Hz. Fig. 5b shows a corresponding numerical pressure signal, measured at the cavity base, for the same duration. The rms of the fluctuations is roughly ±0.09% (G = 1.9): this represents reasonably good agreement between the experiments and the numerics. Note that this numerical amplification involves some statistical uncertainty (roughly ±10%) due to the limited duration of the simulation. Note also that the experimental mean basewall pressure (essentially Pt_2) varies slightly from one run to the next due to wind tunnel tolerances.

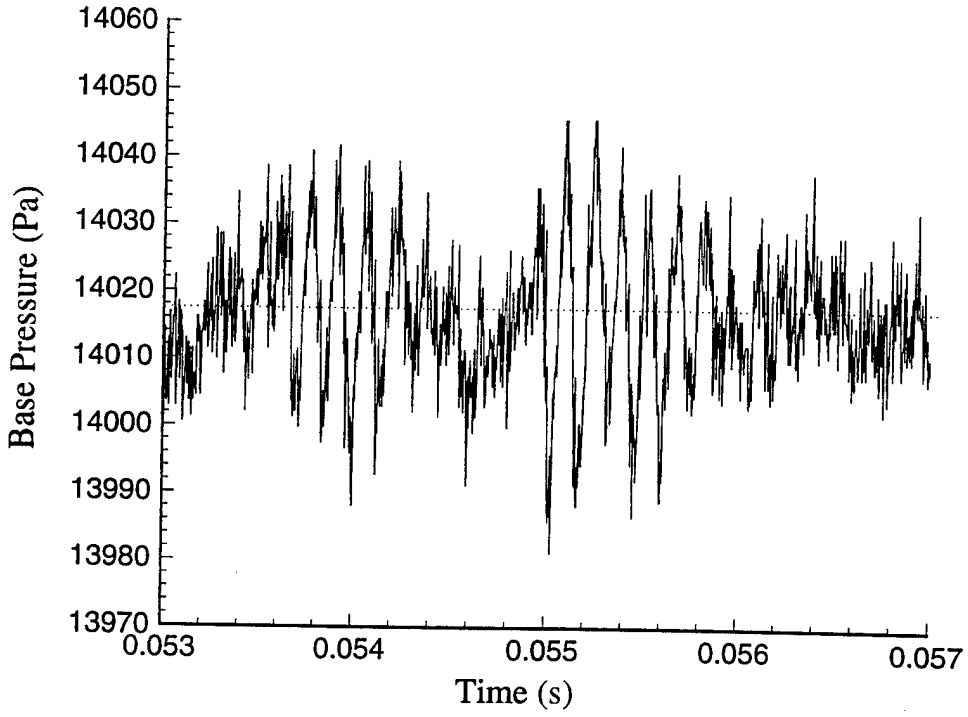

Fig. 5a : Experimental base pressure signal (PQFLT)

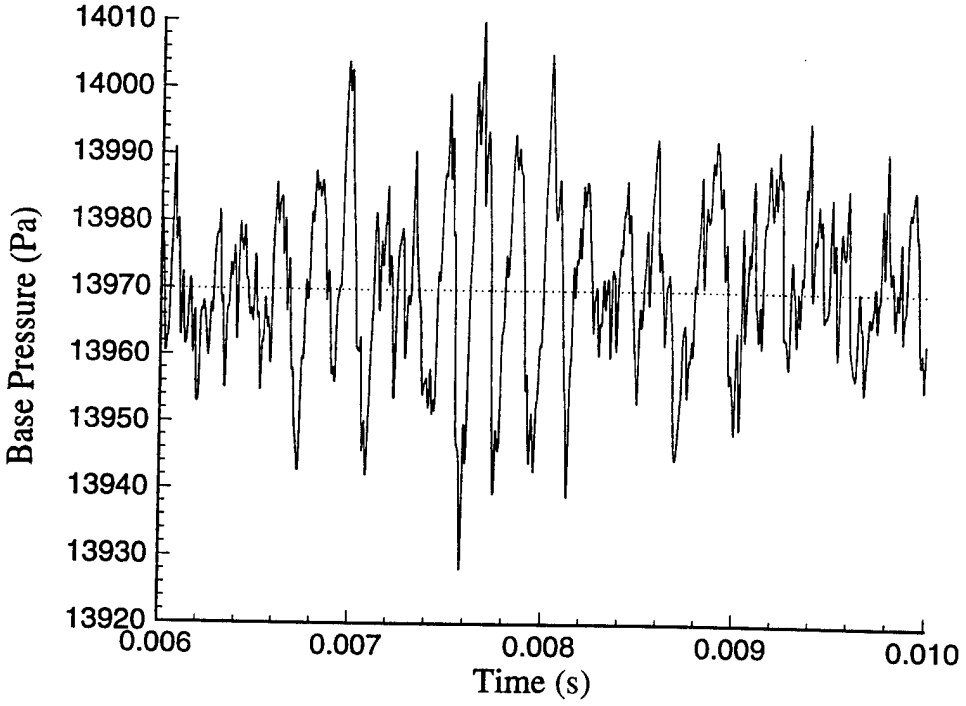

Fig. 5b : Numerical base pressure signal (PQFLT simulation)

A detailed power spectrum of the simulation is difficult to obtain due to the extended signal required. However, it is clear that most of the energy of the oscillations is contained in a primary mode of approximately 6300 Hz. The experimental signal contains more high frequency noise. This is likely because the numerics do not resolve high frequency waves and/or these high frequencies (near 200 kHz) exceed the transducer frequency response and may represent electrical noise.

Fig. 6 illustrates how the amplification grows with cavity *L/D* in the numerical simulations and experiments at both Mach 4 (PQFLT) and Mach 5 (PRC). The numerical and experimental results in PQFLT again show a gradual increase of oscillation strength with cavity depth for relatively shallow cavities ($L/D \leq 1.0$). There is no evidence of a two mode (3-D) behavior mentioned earlier for the Mach 5 experiments in any of the Mach 4 PQFLT results. Note also that the Mach 5 amplification results demonstrate a larger rate of increase with cavity depth than the Mach 4 results. Based on sensitivity results of amplification versus Mach number (discussed later in Section 5.6) it is expected that amplification is somewhat greater at Mach 5. However, the most important conclusion is that these shallow cavities amplify the inflow noise level by roughly the same amount (within a factor of 2) despite the dramatic difference in tunnel noise levels (factor of 24). Consequently, the strength of oscillations for relatively shallow cavities increases with freestream noise level. These results further suggest that broadband freestream tunnel noise is the mechanism of resonance in relatively shallow cavities.

But what is the sensitivity of rms oscillations to frequency content of noise? Time-accurate simulations of Mach 5 flow over a sharp lip, L/D=0.75 nose-cavity (f_1 = 3600 Hz) were conducted using the nominal broadband freestream noise model and a notch filtered freestream noise model (notched from 2400 Hz to 4000 Hz). This filter range was chosen based on a sensitivity study of amplification versus input noise frequency (discussed in section 5.1) to encompas most of the frequency range to which the cavity is sensitive. This cavity produces an amplification of roughly 3.0 (200% increase) when driven by broadband freestream noise. However, the cavity has an amplification of 1.3 (30% increase) when driven by the notched filtered freestream noise. These results demonstrate that relatively shallow cavities only resonate strongly

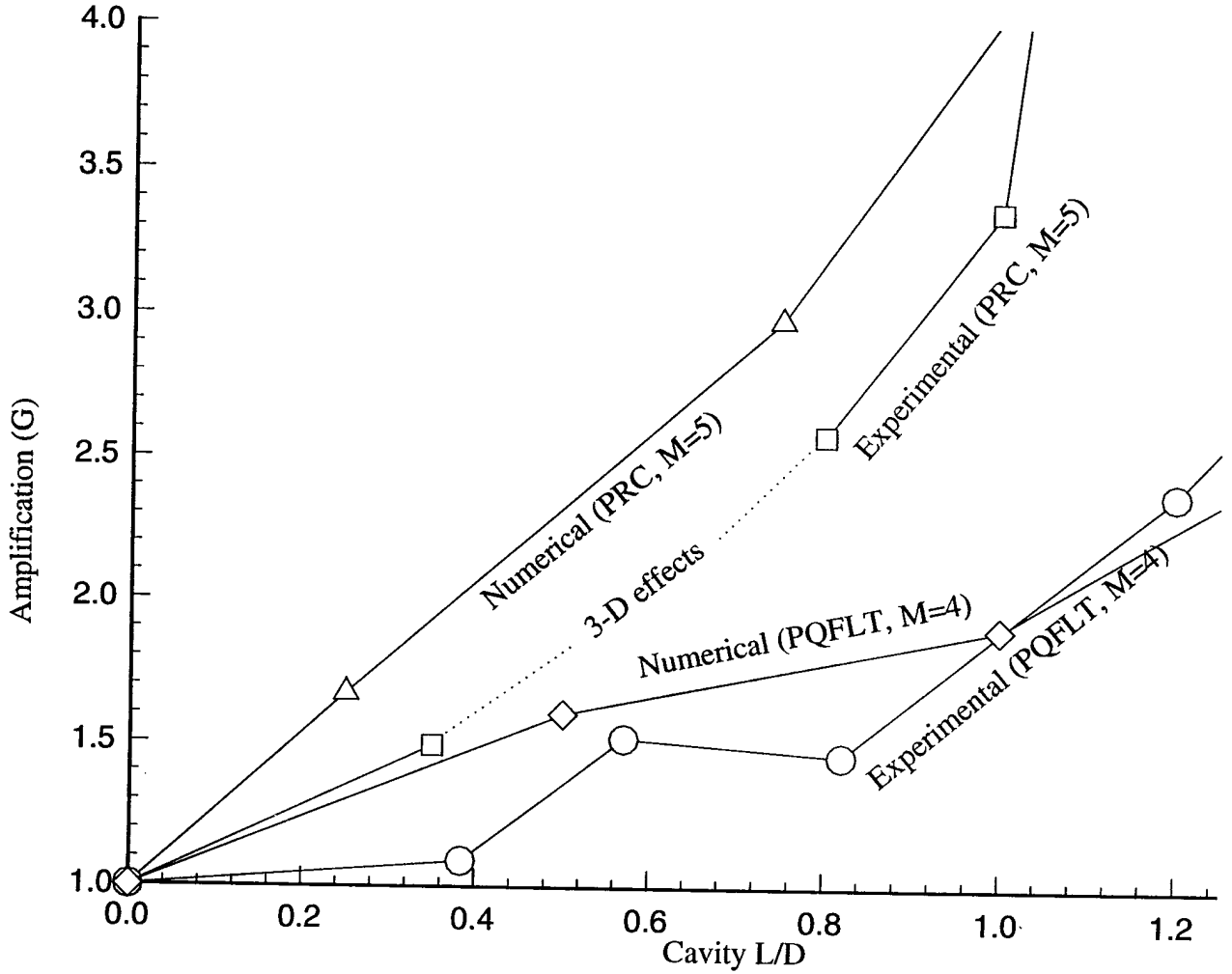

Fig. 6 : Amplification versus tunnel noise level and cavity depth
(Noise levels: PRC = 1.15%, PQFLT = 0.048%)

if the freestream noise contains energy near the primary mode frequency.

4 Spring-Mass-Damper Model

The response of a shallow cavity to inflow noise is somewhat analogous to the response of a damped harmonic oscillator. As just described in Section 3, relatively shallow cavities (L/D < 1.25 @ Mach 5) require the presence of inflow noise containing energy near the characteristic frequency. It will also be shown (Section 5.2) that the strength of oscillations is proportional to the input noise rms (i.e., the amplification remains constant). These features are similar to those of a damped harmonic oscillator which resonates when a periodic forcing function is applied and whose amplitude of oscillations is proportional to input amplitude (i.e., gain is constant). Consequently, it appears plausible that a spring-mass-damper model could be configured to emulate the response of relatively shallow cavities to inflow noise.

Acoustic problems are often modeled using mechanical analogs consisting of lumped elements. The acoustical lumped elements include inductance, compliance, and resistance which are directly related to the mechanical elements of mass, stiffness (represented by a spring), and dissipation (represented by a damper), respectively. The acoustical lumped elements are generally derived from the linearized wave equation, which includes a small disturbance assumption. Specifically, the excess pressure ($|p|$) is assumed small compared to the appropriate static quantity (i.e., $|p| \ll \rho c_o^2$). This assumption is widely used in acoustical analysis and is satisfied in most ordinary acoustic applications. In accordance with the lumped element approximation the characteristic dimensions in the problem must be small compared to the oscillation wavelength (based on the acoustic wave speed). The lumped element approximation is closely related to the assumption that the process is quasi-static (i.e., the entire fluid element changes uniformly in time). For example, the acoustical element of compliance (stiffness) may be derived from the classic short closed cavity problem (Fig. 7a) since the pressure may be assumed constant throughout the cavity at any given time. Similarly, the acoustical element of inductance (mass) may be derived from the classic short open cavity problem (Fig. 7b) since the fluid velocity may be assumed constant throughout the cavity at any given time. Resistance elements are derived in different ways depending on the dissipation mechanism. For example, the radiation resistance

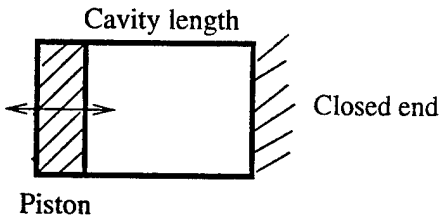

Fig. 7a : Short closed cavity
(cavity fluid is lumped stiffness element)

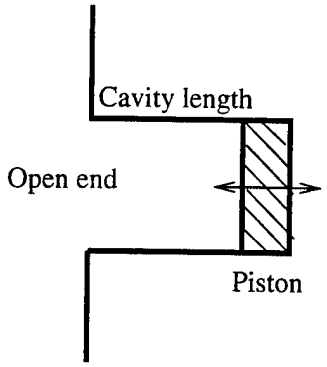

Fig. 7b : Short open cavity
(cavity fluid is lumped mass element)

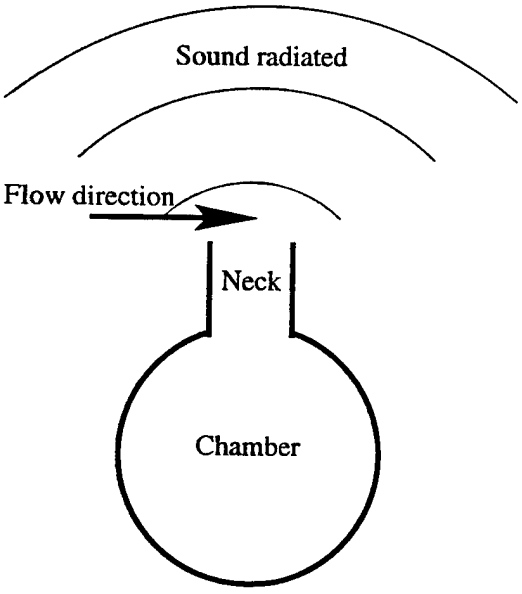

Fig. 7c : Helmholtz Resonator
(infinite medium)

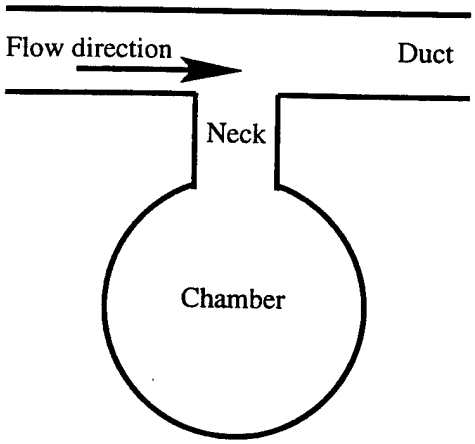

Fig. 7d: Helmholtz Resonator
(finite medium)

element may be derived from a baffled-piston radiating acoustic energy into a semi-infinite medium. For further details concerning the derivation of the various acoustical lumped elements and the mechanical analogs the reader is referred to Blackstock [Ref. 10].

The Helmholtz resonator (Fig. 7c) is commonly modeled as a spring-mass-damper system. The source of the oscillations are input perturbations (acoustic waves traveling into the resonator). For example, input perturbations may be created by crossflow at the inlet which causes periodic vortex shedding at the mouth of the neck. The vortex shedding frequency locks on to the resonator 'quarter-wave' frequency via a feedback mechanism. The resonator typically consists of a short neck attached to a relatively large chamber. The lumped element approximation is reasonable since the oscillation (acoustic) wavelength is typically much larger than the characteristic dimensions (i.e., by a factor of roughly 4). It may be shown that the fluid in the chamber behaves like that in a short closed cavity and is represented by a spring. The fluid in the neck behaves like that in a short open cavity and is represented by a vibrating cylindrical mass. The mass element is typically chosen to have the same radius as the neck and a length of roughly one neck radii. A radiation resistance 'load' is present since the neck fluid vibrates beside an infinite medium. For details and references concerning the Helmholtz resonator the reader is again referred to Blackstock [Ref. 10]. Morse and Ingard [Ref. 11] conclude that if the resonator vibrates into a finite medium (Fig. 7d) then radiation resistance is not present and the main dissipation mechanism is probably due to viscosity.

The hypersonic axial cavity problem can be modeled analogously to the Helmholtz resonator with lumped elements. The small disturbance assumption appears to be reasonably satisfied for weakly-oscillating, relatively shallow, noise-driven cavities ($L/D < 1.25$). Note that this condition is certainly violated for the deeper cavities which produce strong self-sustaining oscillations. The hypersonic axial cavity resembles a Helmholtz resonator except that the cavity must behave as both the neck (mass) and chamber (stiffness). Note that the wavelength is generally greater than four times the cavity length and diameter. Consequently, it may be appropriate to replace the cavity fluid with mass and stiffness elements. However, this analysis does not introduce the necessary numeric mass and stiffness values or the dissipation element.

Consequently, a more intuitive approach is required to produce a mechanical analogy. Specifically, based on time-accurate data and flow animations and the solution to the linearized wave equation, a number of observations are made about the fluid dynamic behavior below. Based on these observations a set of simplifying assumptions is made which lead to the formulation of the basic spring-mass model (see Section 4.2). The dissipation element is added based on further analytical study in Section 4.3. The model is summarized in Section 4.4.

4.1 Fluid Dynamic Observations

As described earlier, inflow noise drives oscillations within relatively shallow cavities; without noise the cavity does not oscillate. Time-accurate flow animations show the fluid dynamic mechanism by which resonance is achieved. Consider a nose-cavity flow simulation involving a sinusoidal model of inflow noise. During one half-cycle the freestream stagnation pressure is larger than the mean value. This positive freestream perturbation results in a larger inflow momentum (and stagnation pressure) reaching the cavity mouth. This relatively large momentum 'encourages' cavity inflow (and increases the pressure gradient within the cavity). During cavity inflow the bow shock is moving downstream, towards the cavity mouth (Fig. 8a). Similarly, negative freestream perturbations result in a smaller inflow momentum (and stagnation pressure) reaching the mouth. This relatively small momentum 'encourages' cavity outflow (and decreases the pressure gradient within the cavity). During cavity outflow the bow shock is moving upstream, away from the cavity mouth (Fig. 8b). Cavity flow reversals occur after each half-cycle. These observations indicate how freestream flow momentum (or stagnation pressure) perturbations are the 'driving force' behind the oscillations.

During start-up (i.e., the first several cycles) both the strength of the pressure oscillations inside the cavity and the bow shock oscillations grow with each input cycle (Fig. 9). Eventually, a pseudo-steady state variation of pressure is reached. The pressure levels within the cavity simply oscillate roughly symmetrically about the steady-state stagnation pressure. The bow shock also oscillates roughly about its steady-state position. During each oscillation cycle the basewall pressure signal reaches a maximum shortly after the bow shock reaches the maximum downstream position.

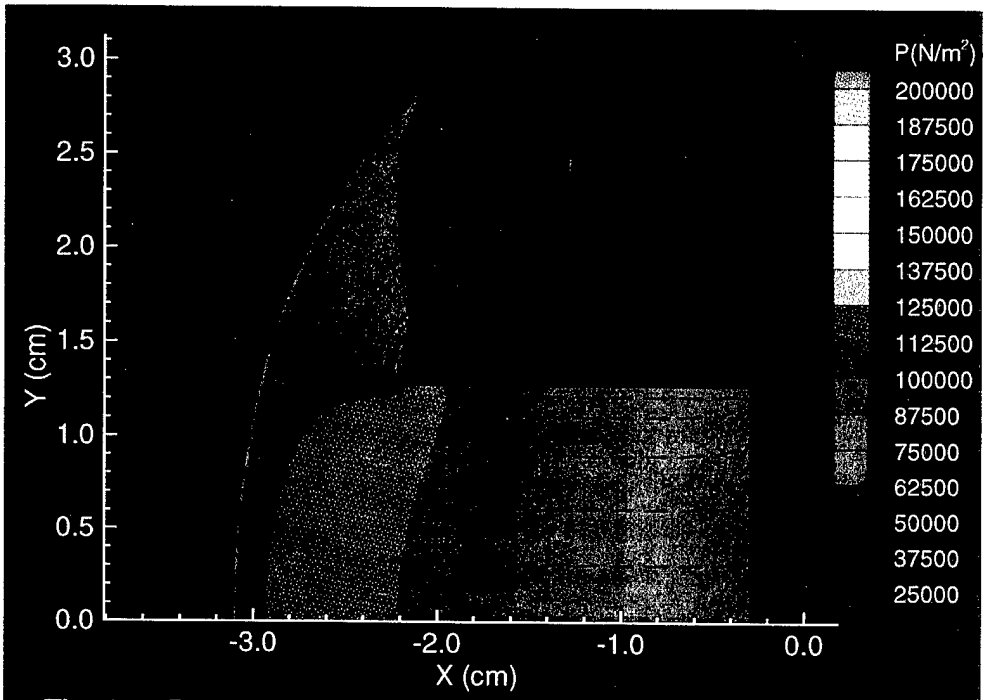

Fig. 8a : Pressure contours (cavity inflow, shock moving aft)
(vectors indicate flow direction) (L/D=0.75, Mach 5, 5% sinusoid)

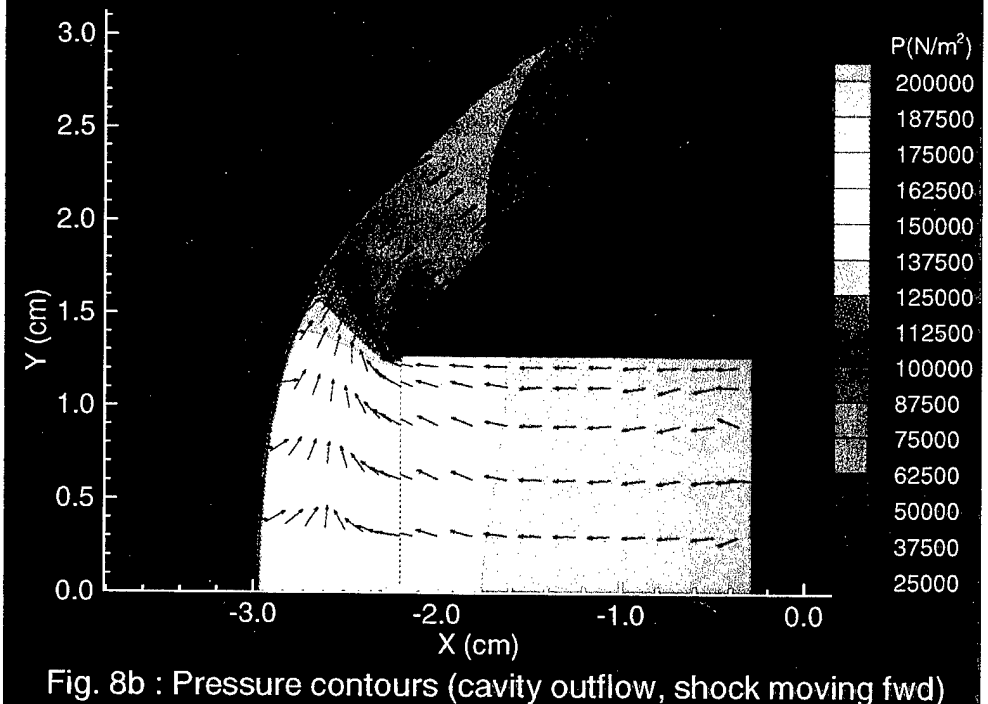

Fig. 8b : Pressure contours (cavity outflow, shock moving fwd)
(vectors indicate flow direction) (L/D=0.75, Mach 5, 5% sinusoid)

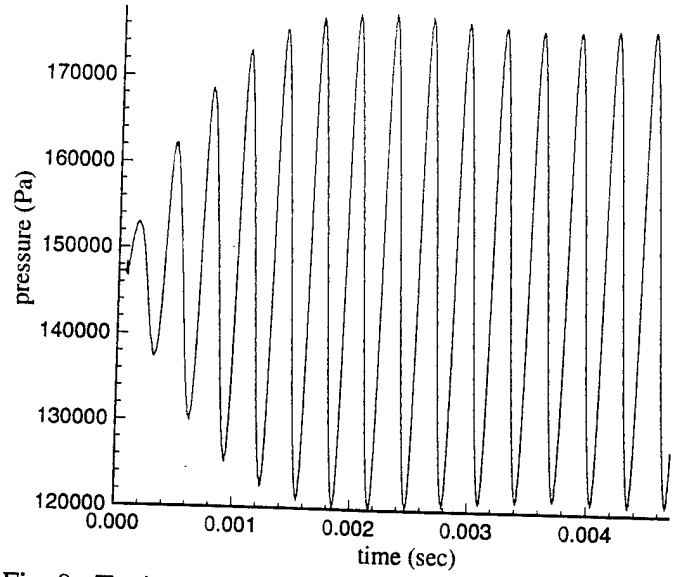

Fig. 9 : Typical base pressure history (sinusoidally-driven)
(L/D=0.75, Mach 5, 2% sinusoid, 3200 Hz)

Specifically, the base pressure signal lags the bow shock oscillations by roughly 45 deg (i.e., 1/8 of an oscillation cycle). Numerical simulations (to be discussed in detail in Section 5.2) also indicate that amplitude of bow shock oscillation increases almost proportionally to basewall pressure amplitude (or rms) for modest strength oscillations. The later observation indicates that the flow exhibits a 'stiffness' since cavity basewall pressure changes proportionally to bow shock movement.

By definition the total mass inside the cavity does not change in a steady flow; the mass flow entering the cavity immediately leaves the cavity. The cavity flow velocities are generally less than Mach 0.1. Consequently, the cavity mass may be estimated using the cavity fluid stagnation density (ρ_{t_2} or ρ_o). In unsteady, time-accurate simulations involving shallow cavities the total mass within the cavity was found to oscillate moderately (e.g., ±20% for L/D=0.75, Mach=5, ±2% sinusoid noise). For simplicity one may assume the cavity mass is roughly constant for these flows.

Figs. 10a and 10b illustrates the absolute and acoustic pressure distributions along the symmetry line at various times during one cycle after the flow has reached a pseudo-steady state. These distributions were obtained from the time-accurate solution

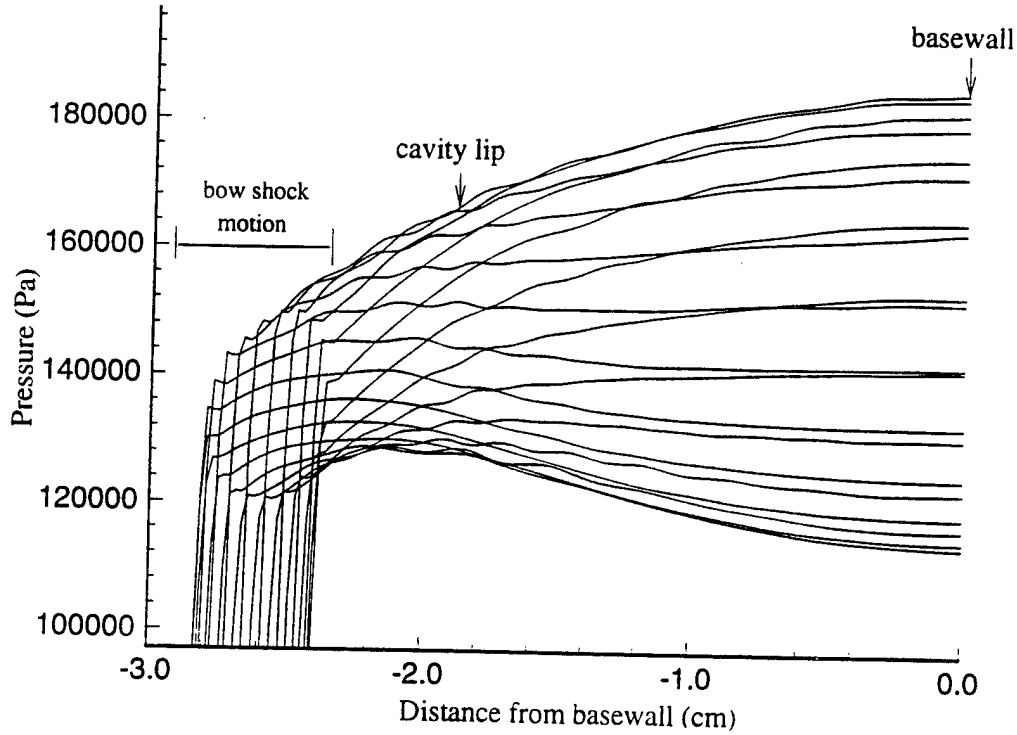

Fig. 10a : Absolute pressure distribution along symmetry line
(20 realizations)

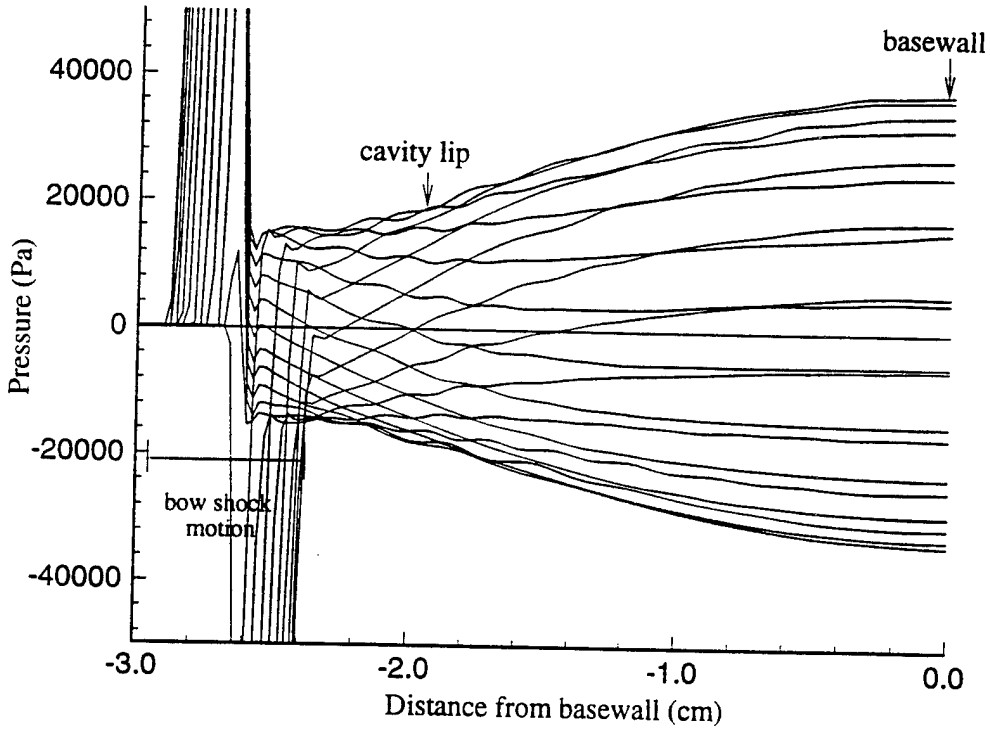

Fig. 10b : Acoustic pressure distribution along symmetry line
(20 realizations)

for a representative case (i.e., L/D=0.75 at Mach 5 driven with ±2% sinusoidal noise at 3400 Hz). The acoustic disturbances are calculated by subtracting the nearly uniform steady flow pressure values from the absolute pressure values. Clearly, the pressure oscillations resemble a quarter-sine wave distribution from the cavity mouth (cavity lip) to basewall at each realization in both plots. The rms pressure levels increase from the lip region and reach a maximum at the cavity base. Careful examination of the absolute pressure distributions reveal that maximum basewall pressure lags the maximum-downstream bow shock position by a phase difference of roughly 45 deg (i.e., 1/8 of an oscillation cycle). This lag is clearly evident in flow animations and implies that the cavity fluid is reacting to freestream perturbations.

Some of these trends are confirmed by linearized wave equation analysis [Ref. 12]. Consider the linearized wave equation for acoustic pressure with appropriate boundary conditions at the bow shock (x=0) and cavity basewall (x=L*):

$$\frac{\partial P}{\partial t} = c^2 \frac{\partial P}{\partial x^2} \qquad P(x=0) = 0, \ \frac{\partial P}{\partial x}(x = L^*) = 0 \qquad (4)$$

By separation of variables a solution is obtained for the acoustic pressure distribution as a function of axial position and time. Substituting this expression into the Euler equation and requiring the acoustic velocity to be zero at the basewall, the acoustic velocity distribution is also obtained. Eqn. 5 contains the acoustic pressure and velocity distributions as functions of axial position (x) and time (t), and τ is the oscillation period:

$$\begin{aligned} P(x,t) &= P_o \sin(\pi x / 2L^*)\sin(2\pi t/\tau), \ \text{where } \tau = 1/f_1 \\ U(x,t) &= U_o \cos(\pi x / 2L^*)\cos(2\pi t/\tau) \qquad (5) \\ P_o &= Z_o U_o, \ Z_o = \rho_o c_o \end{aligned}$$

The acoustic pressure and velocity peak amplitudes, P_o and U_o, occur at the cavity basewall and bow shock, respectively. Note that the spatial pressure distribution follows a quarter sine wave as just described for the CFD solution. The pressure and

velocity amplitudes are related by the characteristic impedance (Z_o) of the fluid, defined above, again implying a fluid stiffness. This analysis confirms the numerical observations described above.

4.2 Spring-Mass Model Formulation

A set of simplifying assumptions, based on the fluid dynamic observations described in the previous section leads to the following model formulation. The stagnation pressure reaching the cavity mouth would be an appropriate choice for a 'driving pressure' in a 1-D spring-mass-damper model. Sinusoidal variations in the freestream static pressure and density lead to sinusoidal variations in the 'driving pressure' in the s-m-d model. Next, assume that the bow shock velocity relative to the body is small (i.e., weak oscillations) so that the relative shock jump conditions are assumed fixed. Consequently, the rms value of the stagnation pressure downstream of the shock normalized by Pt_2 is identical to the freestream static pressure rms value normalized by P_∞. Assume that the stagnation pressure variation (Eqn 6) represents the 'driving pressure' applied at the cavity mouth. The sinusoidal input pressure (P_{in}) is a function of Pt_2 (from normal shock relations), time, input noise amplitude (A), and input noise period.

$$P_{in}(t) = P_{t2}\,[1 + A\,sin(2\pi t/\tau)] \qquad (6)$$

As discussed earlier, for simplicity one may assume the cavity mass and density are roughly constant for weakly-oscillating cavity flows. In the 1-D s-m-d model the cavity fluid mass (per unit area) is estimated using the stagnation density behind a normal shock (ρ_{t_2}) in steady flow and the cavity length:

$$M_{cav} = \rho_{t_2} L. \qquad (7)$$

However, the cavity fluid must also be accelerating nearly uniformly in order that it may be treated as a rigid body (i.e., a mass element). The substantial derivative in the Euler equation represents the total acceleration at a given point and is a function of the local pressure gradient:

$$\frac{Du}{Dt} = -\frac{1}{\rho}\frac{\partial P}{\partial x} \tag{8}$$

for negligible viscous forces.

In order to treat the cavity fluid as a mass element the axial pressure gradient inside the cavity must be assumed constant. As described in the previous section, the axial pressure distribution actually follows nearly a quarter-sine wave distribution at each instant during the oscillation cycle. We approximate the quarter sine wave shape as simply a straight line so a constant *mean* pressure gradient is assumed for the entire cavity.

An expression for the mean pressure gradient is developed as follows. The s-m-d model assumes the input pressure ('driving pressure') is applied at the cavity mouth. The s-m-d model also calculates the basewall pressure (discussed below). The axial pressure distribution inside the cavity then follows a straight line between the two endpoints. The mean pressure gradient is the same for quarter-sine and linear distributions which share the same endpoints:

$$\left(\frac{\partial P}{\partial x}\right)_{mean} = \frac{P_{base} - P_{in}}{L} \tag{9}$$

The sum of pressures on the cavity fluid mass element is then easily found using Eqn. 8 and some manipulation:

$$\sum P = P_{in} - P_{base} \tag{10}$$

The final unknown in the spring-mass model is the cavity basewall pressure (P_{base}) which may also be found from fluid dynamic observations. The base pressure amplitude appears to grow *proportionally* to the bow shock amplitude for a given nose-cavity geometry for weak to moderate oscillations (see Section 5.2). This behavior indicates a fluid stiffness. Moreover, this stiffness is reduced as cavity depth is increased in that the base pressure amplitude grows more slowly with bow shock displacement amplitude. This trend confirms the common experience that pushing a

piston into a deep cavity is easier than pushing it into a shallow cavity. Consequently, the basewall pressure is modeled using a spring relation.

The basewall pressure (or 'spring force') is calculated based on the cavity stiffness (k) and the current deviation of the bow shock position (x-x_O) from its steady-state equilibrium position:

$$P_{base} = k(x - x_o), \text{ where } x_o = P_{in}/k \qquad (11)$$

Recall that the natural frequency of a spring-mass-damper system is a function of the mass (already known from Eqn. 7) and stiffness. The natural frequency (f_1) of any given nose-cavity may be calculated from Eqn. 2. So, the stiffness is easily obtained as follows by substituting values for the mass and natural frequency:

$$k = (2\pi f_1)^2 m_{sys} \qquad (12)$$

The current bow shock position (x) is estimated using the current mass element position (the bow shock is assumed fixed to the mass). Steady flow conditions (i.e., 'spring force' equals the input force) are used to set the initial shock position (x_O), see Eqn. 11.

There is a relatively small additional mass element that should be added to the cavity mass element to account for cavity mouth effects on the system mass:

$$m_{sys} = m_{cav} + \Delta m \qquad (13)$$

The details regarding this additional mass element are provided in the discussion of the dissipation coefficient in the next section.

4.3 Dissipation Mechanism

The dissipation mechanisms which damp cavity oscillations are assumed to include those commonly listed for the Helmholtz resonator [Ref. 10]: fluid viscosity, wall heat transfer, and radiation of acoustic energy. It is reasonable to believe that there may also be a mechanism associated with shock motion. One can imagine viscous wall forces tending to retard the motion of the cavity fluid as it moves back and forth. Wall

heat transfer can also cause dissipation since compression and expansion which occurs during the oscillations tends to be isothermal, not adiabatic, in the thermal boundary layer. Dissipation and dispersion of acoustic waves caused by viscous forces and heat transfer within the boundary layer can be estimated for a cylindrical cavity based on wave equation analysis [Ref. 10]. There are also thermoacoustic effects [Ref. 13] in which the heat transfer to the wall is different during compressions than during expansions thereby creating a net heating or cooling effect which may affect oscillation strength. A related effect is the net heating of the wall which occurs during compression/expansion since the thermal conductivity of air increases with temperature. However, numerical simulations for a representative nose-cavity case with and without fluid viscosity (see Section 5.7) and with and without wall heat transfer (see Section 5.8) indicate negligible differences in the resulting pseudo-steady pressure oscillations. Consequently, viscous and thermal wall effects do not appear to be the primary dissipation mechanisms for the hypersonic axial nose-cavity.

The primary dissipation mechanism appears to be associated with radiation of acoustic energy from the cavity mouth, as in many other acoustic devices which include an open tube (e.g., Helmholtz resonator into an infinite medium). When sound energy reaches the end of a short tube some of the acoustic energy is reflected back into the tube while some is *radiated* into the fluid outside the tube. Typically the effect of radiation from the end may be approximated by assuming a small layer of fluid oscillates at the cavity mouth like a piston. For the present geometry, the body outer surface acts as an annular flange or baffle. Hence, the acoustic behavior is represented by a baffled-piston. Flow animations clearly show acoustic waves radiating from the cavity mouth into the semi-infinite field. Although acoustic energy is reflected by the bow shock, some acoustic energy leaving the mouth radiates radially and downstream, representing energy dissipation. Also, the discussion in Section 4.1 confirms that the fluid at the cavity mouth accelerates almost uniformly and can be treated as a lumped mass element which vibrates like a piston. Consequently, there is strong evidence that the principal dissipation mechanism is related to the baffled-piston radiation effect.

4.4 Baffled-Piston Radiation Model

Attempts to analytically model the baffled-piston radiation effect present in the hypersonic axial cavity problem are described below. First, analytical results from the classic baffled-piston problem are applied to the present problem. Then a baffled-piston image problem is developed to investigate the effect of bow shock reflections in the present problem. A different dissipation argument, based on the spherical spreading of acoustic energy between the cavity mouth and bow shock, is also presented. Finally, an experimentally-derived dissipation trend is briefly discussed. A functional relationship for the dissipation element within the spring-mass-damper model is chosen based on the trends established by the analytical work.

The baffled-piston oscillating beside a semi-infinite medium (Fig. 11a) is a classical acoustic problem in which the piston radiates into a uniform, semi-infinite domain. In the classic problem an analytical expression for the complex pressure field is calculated by integrating the effect of simple sources representing the vibrating surface at each point in the field. The complex impedance at the piston face ($Z_p = Z_r + iZ_i$) is calculated by dividing the mean pressure amplitude (P_o) over the piston face by the piston velocity amplitude (U_o). The real part of the impedance (Z_r) represents the radiation resistance for the acoustic system, which is analogous to the dissipation coefficient (b) in a mechanical system. The imaginary part (Z_i) represents the acoustic inductance, which is analogous to a mass element in a mechanical system. Fig. 11b illustrates the variation of the real (R) and imaginary (X) coefficients of the radiation impedance (i.e., real and imaginary parts normalized by Z_o) with the wave number ($wn = 2\omega D/c_o$, where D is the cavity diameter and w the oscillation frequency). The wave number is essentially a non-dimensionalized frequency. In the low frequency limit ($wn = 0$) the resistance coefficient is zero. No acoustic energy is transmitted to the semi-infinite field. In the high frequency limit the coefficient is approximately one (i.e., the resistance is equal to the characteristic fluid impedance, Z_o). All of the acoustic energy is radiated to the semi-infinite field.

Suppose now that the hypersonic axial cavity flow problem contains a baffled-piston radiating into a semi-infinite medium (i.e., ignore the bow-shock). The

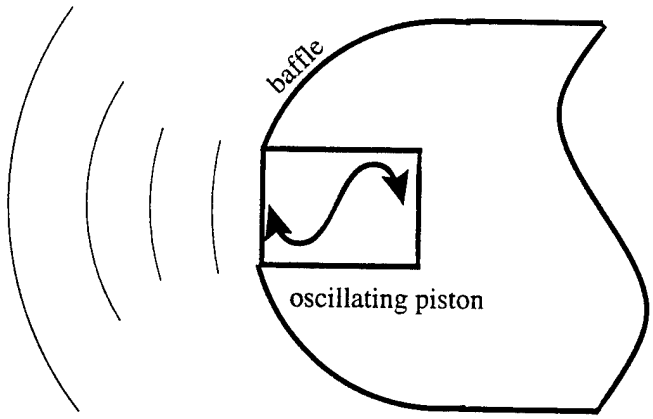

Fig. 11a : Baffled-piston radiating into a semi-infinite medium

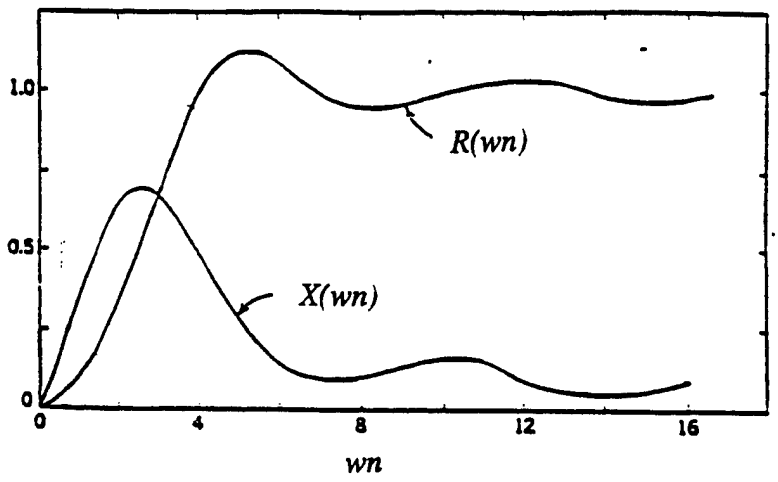

Fig. 11b : Baffled-piston radiation resistance and inductance (Ref. 41)

characteristic impedance in the hypersonic axial cavity problem corresponds approximately to the stagnation conditions ($\rho_o c_o$). Substituting Eqn. 2 for the wave number it is easily shown that $wn = \pi D/2L^*$. Substituting an appropriate range of L^*/D values for relatively shallow cavities at Mach 5 (i.e., $0.25 < L/D < 1.25$), the corresponding range for the wave number is roughly in the range 1 to 3. In this 'medium' range resistance coefficient (R) increases almost linearly with wave number radiation. Consequently, assuming the hypersonic cavity flow problem resembles a baffled-piston radiating into a semi-infinite medium, one could approximate the dissipation as a linear function of wave number (or D/L^*):

$$b = c_1 Z_o (D / L^*) \quad \text{where } c_1 \text{ is a constant} \qquad (14)$$

However, radiation in the hypersonic axial cavity flow problem is significantly more complicated than the classic baffled-piston problem. A major complication is posed by the bow shock which will reflect and invert acoustic waves. The strong convection current just outside the cavity mouth would significantly distort the acoustic waves between the cavity mouth and bow shock. The effect of shock motion, curvature, and proximity to the mouth would also have a pronounced effect on the acoustic field. The spring-mass-damper model presented herein focuses on relatively shallow cavities which do not oscillate strongly. The model attempts to account for the effect of shock reflection on the dissipation mechanism (discussed below) and puts aside to qualitative discussion the effects of convection currents and shock motion.

There is good reason to believe that radiation resistance decreases as the mean bow shock position moves close to the cavity mouth. The bow shock appears to reflect and invert acoustic energy back towards the cavity mouth, reducing acoustic energy losses. There is experimental evidence that solid reflectors near a baffled-piston increase acoustic output. For example, hartmann whistle researchers found that annular reflectors around the jet tended to increase acoustic efficiency [Ref. 14].

A brief analysis of a baffled-piston image problem (Fig. 12a) provides one possible explanation of shock reflection effects. One baffled-piston represents the oscillating cavity mass (i.e., the source). Another equal-strength image baffled-piston

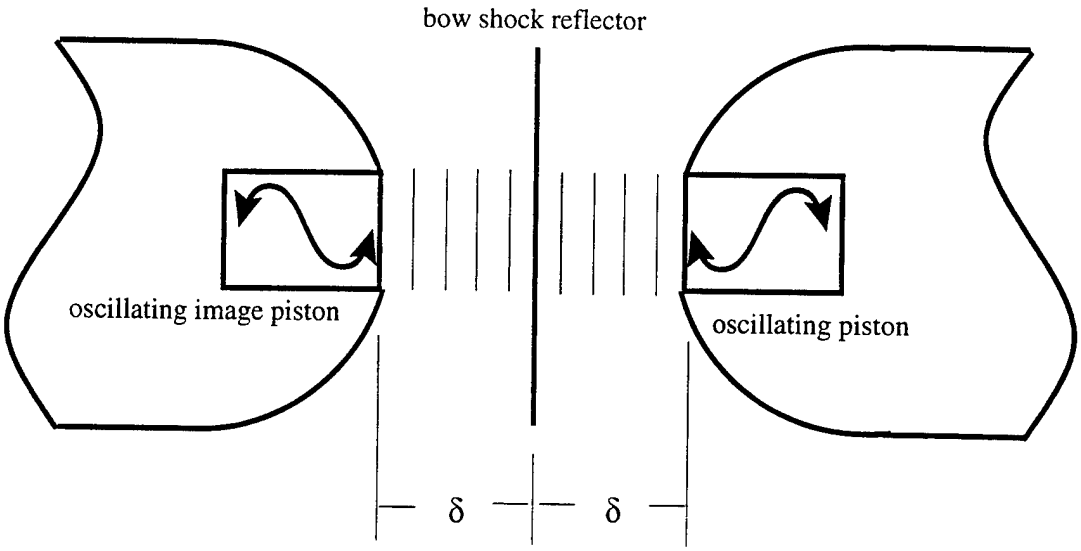

Fig. 12a : Image-pistons schematic

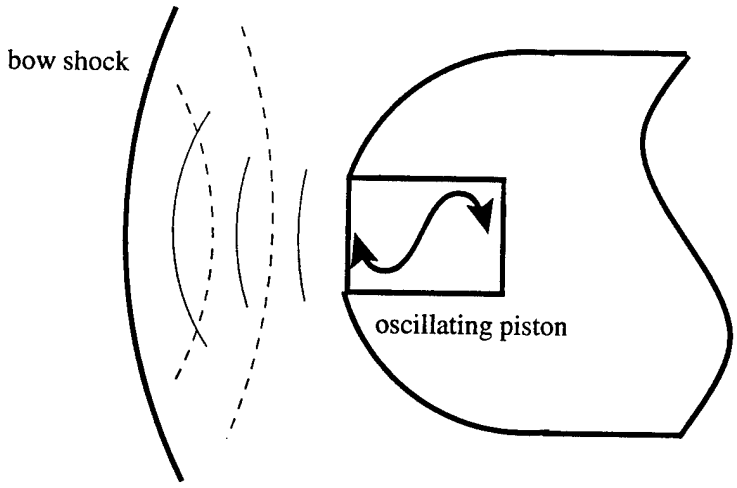

Fig. 12b : Spherical spreading ('decay') argument

oscillates at the same frequency, and 180 deg out-of-phase (i.e., a sink), and faces the first piston along the symmetry line. The pistons are separated by twice the standoff distance (δ). The acoustic pressure field is calculated by superimposing the acoustic fields produced by each piston alone. The resulting acoustic pressure at the bow shock is zero (a node point). As in the classic baffled-piston problem described earlier the real part of the impedance (Z_r) at the oscillating piston face represents the radiation resistance or dissipation (b).

An analytical expression for the impedance at the source piston face is obtained by making the simplifying assumption that the baffled-piston radiates all acoustic energy as plane waves towards the bow shock without spherical spreading ($R = 1$). This assumption is equivalent to assuming the effect of piston radius is small. For the classic baffled-piston problem it may be shown that spherical spreading is not established until an axial distance of greater than the piston diameter. In the nose-cavity configurations traveling the maximum axial distance of wave travel from the piston is the shock standoff distance and this is smaller than the piston diameter. Consequently, the assumption of plane waves between the bow shock and cavity mouth appears reasonable provided the effects of strong convection are ignored. The resulting plane wave solution for the complex pressure field, $p(x,t)$, due to a single baffled-piston is a function of the pressure amplitude (P_o), the oscillation frequency (f), wave speed (c_o), time (t), and axial distance from the vibrating surface (x):

$$p(x,t) = P_o \, e^{\,i2\pi(ft - fx/c_o)} \tag{15}$$

The analytical expression for the complex pressure field at the piston face is found by superposition of the complex pressures produced by the source piston ($x = 0$) and the image piston ($x = 2\delta$). Dividing by the velocity expression for the sinusoidally-oscillating piston we obtain the complex impedance at the piston face:

$$Z_p = Z_o \left[\left(1 - cos\left(4\pi\delta f/c_o\right)\right) + i \left(sin\left(4\pi\delta f/c_o\right)\right) \right]. \tag{16}$$

Substituting for the oscillation frequency (f) using an expression similar to Eqn. 2 based on a length scale (L_f) the final expression for impedance is obtained as:

$$Z_p = Z_o\left[\left(1-cos(\pi\delta/L_f)\right)+i\left(sin(\pi\delta/L_f)\right)\right]. \qquad (17)$$

Note that if the frequency is set equal to the primary frequency from Eqn. 2 then L_f becomes L^*.

The real part of the impedance at the piston face is proportional to Z_0 and varies roughly quadratically with the non-dimensional parameter δ/L_f for moderate values of δ/L_f (i.e., for relatively shallow cavities). Note, acoustic waves generated at the cavity mouth travel one standoff distance, reflect off the shock, and return to the cavity mouth, assuming the wave speeds and amplitudes are not appreciably affected during transit. These reflected waves could interfere with piston motion since the returning waves may be out-of-phase with the piston. Theoretically, if the shock is fixed at the cavity mouth there is no acoustic pressure (or dissipation) at the piston face. Consequently, the ratio of the standoff distance to the length scale associated with the oscillation frequency appears to be an important parameter in the calculation of radiation resistance. Based on the image-piston problem a reasonable approximation for the radiation resistance is given by:

$$b = c_1\, Z_o\left(\delta/L_f\right)^2 \qquad (18)$$

Recall that based on the classic single baffled-piston problem the same functional relationship could be assumed (except replacing δ with D as shown in Eqn. 15).

Another argument can be made that dissipation should increase with bow shock standoff distance. If the standoff distance is relatively large the bow shock would 'see' the cavity mouth as an acoustic point source. The acoustic waves would spherically spread before reaching the bow shock (Fig. 12b). That is, acoustic energy would be dissipated between the cavity mouth and bow shock due to radial spreading. Consequently, it is reasonable to expect that dissipation increases with standoff distance.

Finally, recent results from an experimental study [Ref. 15] of strongly-perturbed cavity flows at Mach 4 (PQFLT facility) focused on the ability of a given cavity to dissipate strong oscillations. In the experiments a Nd:Yag laser is used to introduce controlled thermal-acoustic perturbations upstream of the cavity mouth. These 'hot-spot' perturbations induce strong oscillations within the cavity which dissipate over a period of several oscillation cycles. Based on the observed dissipation rates of the pressure oscillations at the cavity base an exponential decay rate (and damping coefficient) is fit to the data. The damping coefficient was found to decrease quickly with the characteristic length scale (i.e., $b \sim 1/L^{*2}$) for $L/D < 2.0$. Note that this trend is based on only four cavity depths and does not provide a complete functional relationship for the dissipation element.

Based on the analytical arguments just described it would seem reasonable to assume the radiation resistance in the spring-mass-damper model is related to the characteristic fluid impedance (Z_0) and bow-shock standoff distance (δ), and inversely related to the length scale associated with oscillation frequency (L_f). The constant of proportionality, c_1, is 'calibrated' for a representative cavity configuration. Assuming a *proportional* relationship, the resulting equation for radiation resistance is then:

$$b = c_1 \, Z_o \left(\delta / L_f \right) \tag{19}$$

When an oscillating cavity is modeled as a baffled-piston vibrating into either an infinite or finite medium, an acoustic inductance (or mass element) is usually included to represent a small layer of fluid just outside the cavity mouth [Ref. 10]. The added mass can be calculated from the classic baffled-piston problem, even when a reflector is present. Suppose the piston emits plane waves, as assumed in the derivation of the dissipation element (i.e., piston vibrates at the high frequency limit). The imaginary impedance coefficient (X) for a baffled-piston at the high-frequency limit is 0.2 (see Fig. 11). To obtain the added mass value (Δm) this coefficient must be divided by the wave number (based on the oscillation length scale).

$$\Delta m = 0.127 \rho_o L_f \tag{20}$$

This added mass (per unit area), however, only has a secondary effect on the s-m-d model results.

4.5 S-M-D Model Summary

The fluid dynamic response of a relatively shallow cavity to sinusoidal freestream perturbations is approximated by a spring-mass-damper model (Fig. 13). The entire cavity fluid is assumed to accelerate like a rigid mass (m_{cav}) based on the one-dimensional Euler equation (assuming a constant density and a mean axial pressure gradient). The mean axial pressure gradient is derived assuming a linearized quarter-sine wave axial pressure distribution and is simply a function of the input pressure at the cavity mouth (P_{in}), the base pressure (P_{base}), and the cavity length (L). Substituting for the pressure gradient in the Euler equation and rearranging, the following simple relation is obtained for the sum of pressures on the mass element:

$$\sum P = P_{in} - P_{base} \tag{21}$$

The input pressure is the driving pressure and is represented by the time-varying stagnation pressure behind the bow shock. The base pressure is calculated based on an approximate cavity fluid stiffness (k) and the bow shock displacement from its steady flow position (x_{sh} - x_O). Note, the bow shock motion (i.e., displacement (x_{sh}), velocity (V_{sh}), and acceleration ($\dot{V}_{sh}$)) and the rigid mass motion are assumed identical in the s-m-d model. Consequently, there is no phase difference between the maximum basewall pressure and the maximum downstream position of the bow shock although there was a modest phase difference in the CFD simulations of roughly 1/8 of an oscillation cycle. The dissipation (b) appears to be associated with radiation of acoustic energy from the cavity mouth and is derived from a baffled-piston image problem. A small additional mass element (Δm) is included in the total mass element (m_{sys}) to represent the inertance at the cavity mouth associated with baffled-piston radiation.

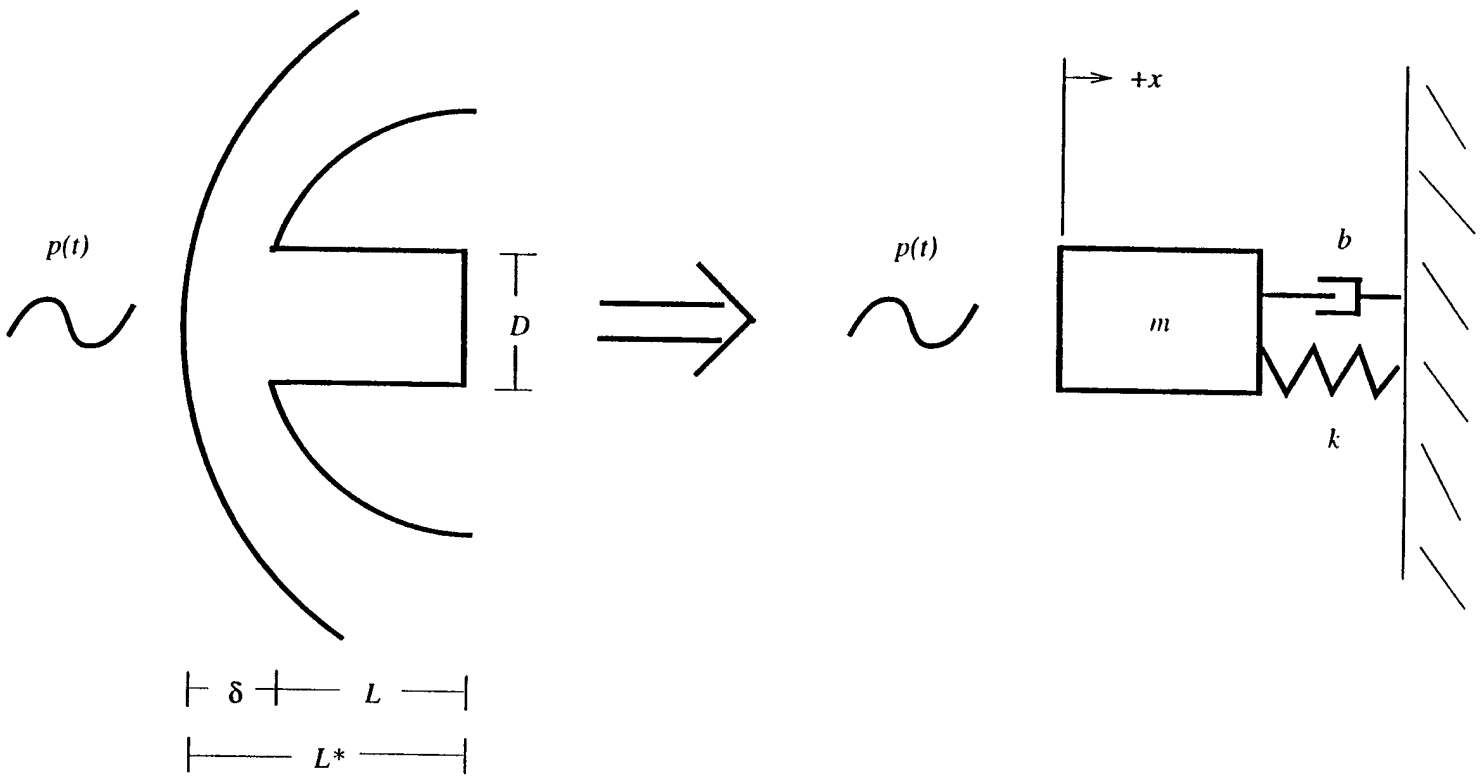

Fig. 13 : Spring-mass-damper model schematic

Adding the dissipation into Eqn 21 and rearranging, the following second order linear system (two first order ODEs) is derived:

$$\begin{aligned} \dot{x}_{sh} &= V_{sh} \\ \dot{V}_{sh} &= (P_{in} - k(x_{sh} - x_o) - bV_{sh})/m_{sys} \end{aligned} \tag{22}$$

A small program was used to used to solve these equations.

In the program the user selects the model geometry (cavity length, cavity diameter, body nose diameter), mean freestream static conditions (velocity, temperature, pressure), and a noise model (frequency and amplitude). The program calculates the shock stand-off distance based on the Mach number and body nose diameter using an empirical relation from Anderson [Ref. 16]. Eqn 2 is then used to calculate a natural frequency. Next, the mass, stiffness, and dissipation elements are calculated using the relations described earlier (repeated below in Eqn. set 23). The initial bow shock position (x_o) is set based on steady flow conditions. Specifically, the spring force is set equal to the steady flow input pressure (i.e., stagnation pressure behind a steady normal shock). The damping calibration constant (c_1) is set to 0.40 to provide best agreement with one representative CFD simulation (i.e., specific geometry, inflow conditions, noise configuration).

$$\begin{aligned} m_{cav} &= \rho_{t2} L; \\ \Delta m &= 0.127 L_f; \\ m_{sys} &= m_{cav} + \Delta m \\ k &= (2\pi f_1)^2 m_{sys}, \\ x_o &= P_{in}/k \\ b &= c_1 Z_o (\delta / L_f) \end{aligned} \tag{23}$$

The two first order differential equations(22) describing the second order linear system are integrated in time using a 4th order Runge-Kutta scheme. The model calculates the input pressure based on the current time. The sinusoidal inflow noise model is repeated below as Eqn. 24:

$$P_{in}(t) = P_{t2}\,[1 + A\,sin(2\pi t/\tau)] \qquad (24)$$

Once the oscillations are pseudo-steady the model calculates the amplification (Eqn. 3) and average bow shock speed to provide direct comparison with CFD simulation results.

5 Sensitivity Study (CFD vs. S-M-D)

A sensitivity study of relatively shallow cavities (L/D < 1.25) is conducted in order to understand how different parameters affect the strength of oscillations within the cavity. In all sensitivity cases examined numerical resonance is simulated by input of sinusoidal freestream noise at a discrete frequency.

The nominal case is a medium depth cavity (L/D=0.75) with a sharp lip. The inflow noise peak-to-peak amplitude of pressure and density are ±0.02 P_∞ and ±0.02 ρ_∞, respectively. The mean freestream conditions correspond to those in the Mach 5 facility. Note that the freestream rms amplitudes are 1.41%. The simulation results for the nominal case serve as a standard for comparison to the other cases.

The sensitivity of amplification to various parameters is determined using both INCA and the spring-mass-damper (s-m-d) model. The parameters studied with INCA include noise frequency, noise amplitude, noise variable type, cavity depth, cavity lip radius, body nose diameter, Mach number, fluid viscosity, and thermal wall condition. The parameters studied with the s-m-d model are a subset of this list and include noise frequency, noise amplitude, noise variable type, cavity depth, body nose diameter, and Mach number but neglect cavity lip radius, fluid viscosity, and thermal wall condition. The validity of the s-m-d model is studied by directly comparing th model and CFD results.

5.1 Sensitivity of Amplification to Noise Frequency

Consider first the dependence of pressure amplification (G), defined in Eqn. 3, on input perturbation frequency. Fig. 14 illustrates the variation of amplification with input frequency for the nominal case (L/D = 0.75 @ Mach 5) using both INCA and the s-m-d model. There is a strong dependence of the amplification on input frequency. The amplification is maximum when the driving frequency (f) is a particular value (f_{opt}). This optimum frequency is slightly less than the primary frequency from Eqn. 2 (3650 Hz) using both CFD (8% lower) and the s-m-d model (1% lower). Using both CFD and SMD, the amplification also drops rapidly (rolls-off) with changes in the driving frequency. The curve is more rounded near the peak for the CFD results which suggests that axial cavity flow behavior cannot be emulated precisely with a linear s-m-d system. As discussed earlier, the s-m-d model is calibrated using the optimum amplification value for this nominal case (i.e., $c_1 = 0.4$). It is important to note that this constant is the same for all cases and was set using just this one CFD amplification result.

Fig. 15 shows the dependence of amplification on input frequency for three cavity depths (L/D=0.25, 0.75, and 1.25) near the amplification peaks for both INCA and the s-m-d model. These peaks become higher and sharper as cavity depth (and amplification) is increased. The increase of normalized amplification roll-off, $|dG/d(f/f_{opt})|$ with amplification is consistent with a damped harmonic oscillator.

Fig. 16 presents basewall pressure histories from start-up for the L/D=0.25 and 0.75 cases driven at f_{opt} for both INCA and the s-m-d model. Note the good agreement between the CFD and s-m-d histories. The first pressure peak is nearly the same for both cavity deptths, which is expected since the acoustic input energy (i.e., rms) is identical.

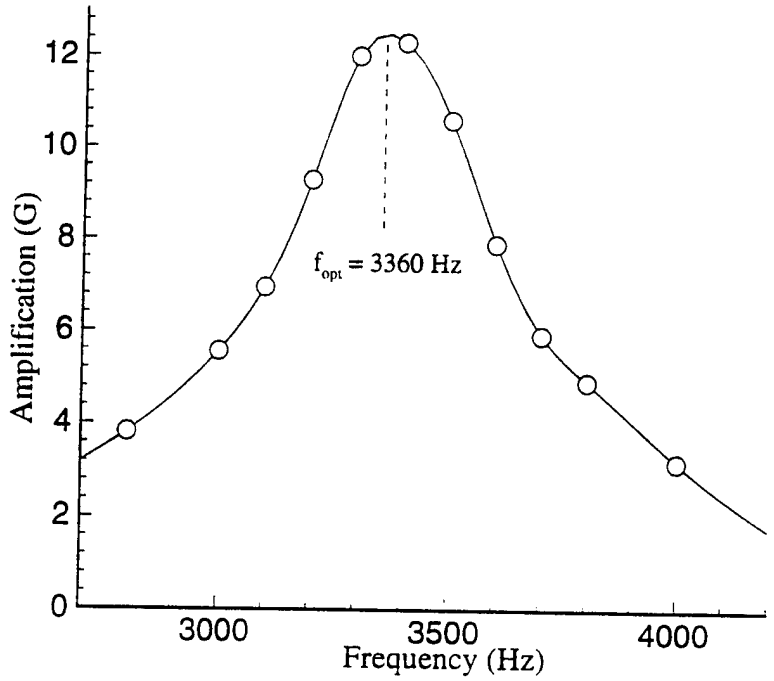

Fig. 14a : Amplification vs. driving frequency (nominal case, CFD)

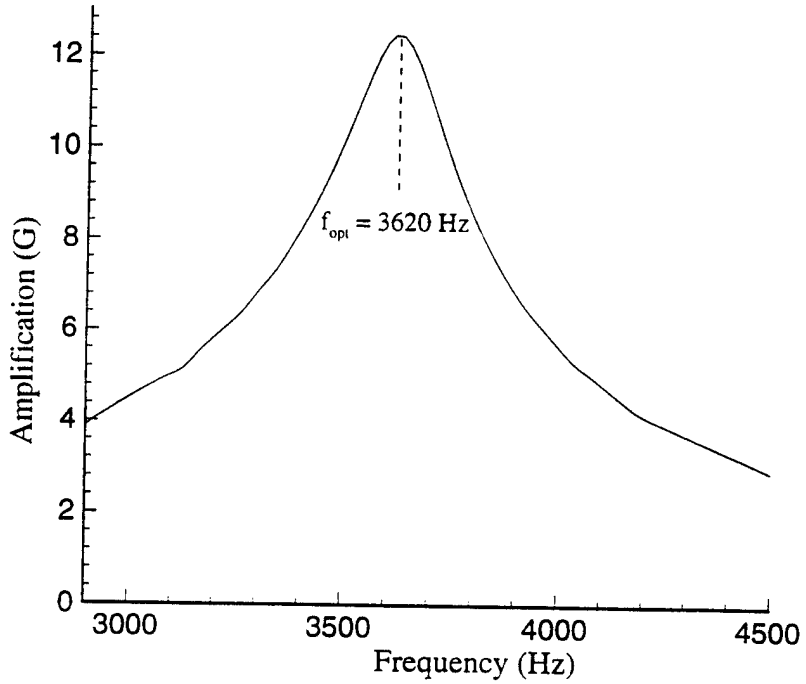

Fig. 14b : Amplification vs. driving frequency (nominal case, S-M-D)

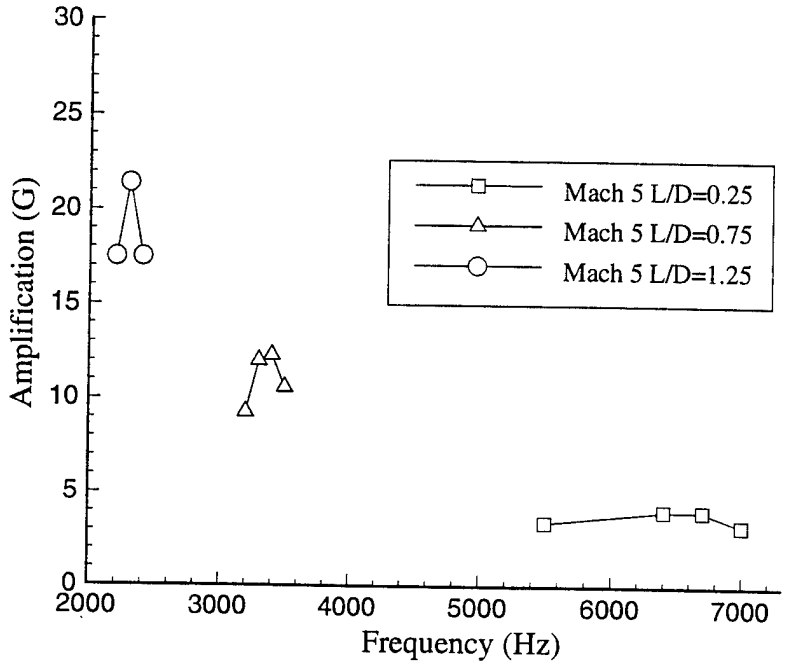

Fig. 15a : Peak amplification vs. driving frequency (CFD)

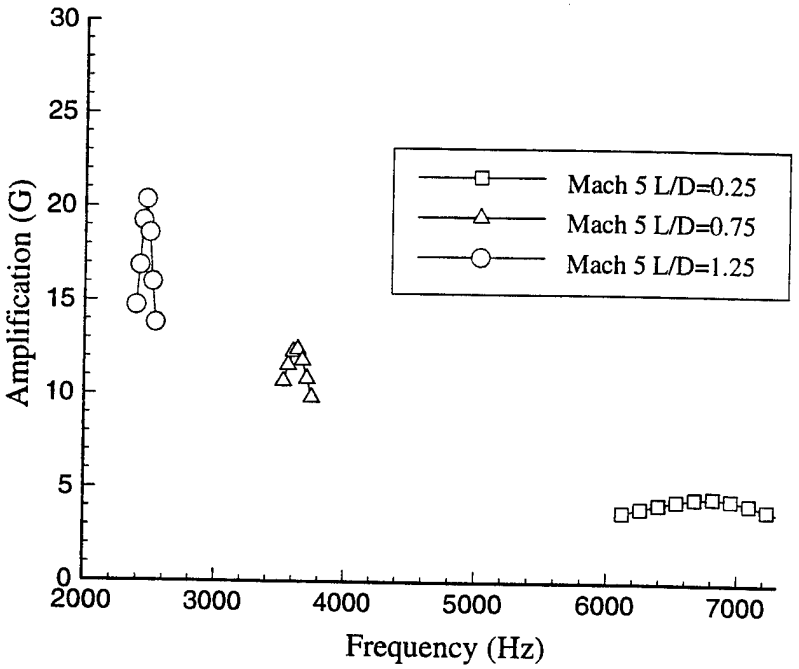

Fig. 15b : Peak amplification vs. driving frequency (S-M-D)

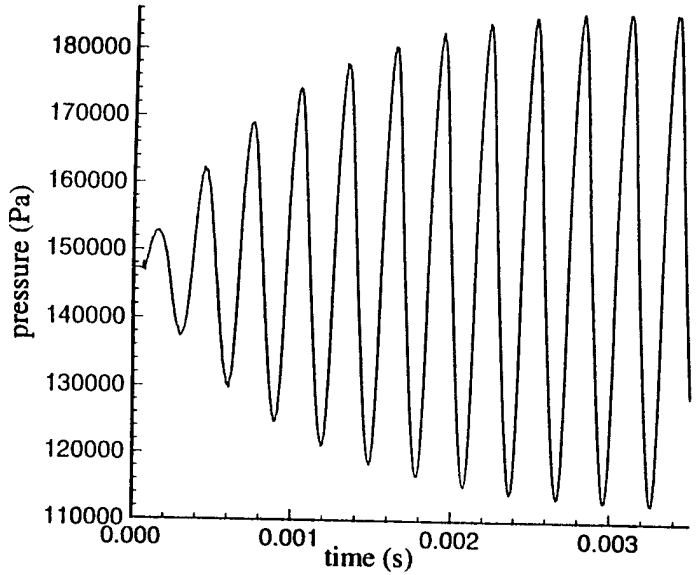

Fig. 16a : Basewall pressure history (L/D=0.75, CFD)

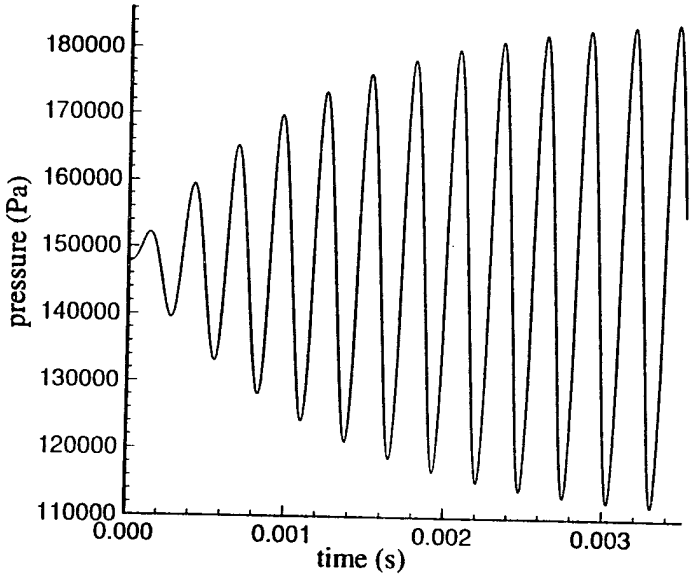

Fig. 16b : Basewall pressure history (L/D=0.75, S-M-D)

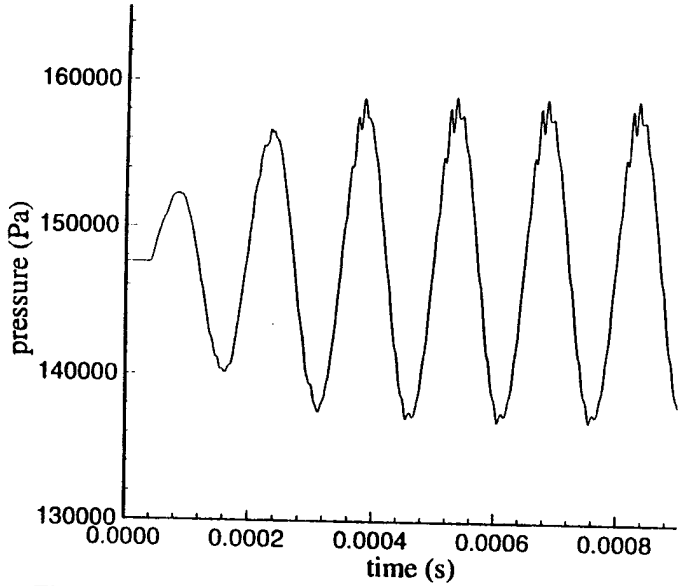

Fig. 16c : Basewall pressure history (L/D=0.25, CFD)

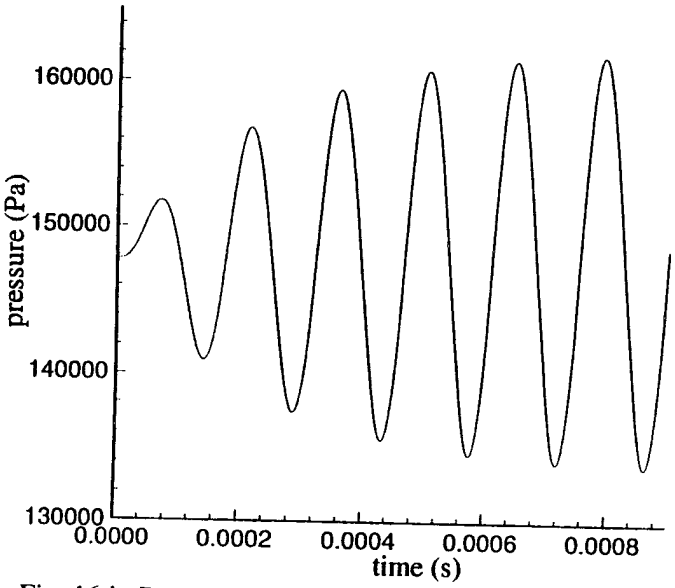

Fig. 16d : Basewall pressure history (L/D=0.25, S-M-D)

5.2 Sensitivity of Amplification to Noise Amplitude

Consider the dependence of amplification on noise level (i.e., input perturbation amplitude). Several simulations are performed for the nominal L/D=0.75 configuration at different noise amplitudes using different frequencies to isolate the frequency which provides maximum amplification. In each case the same frequency (3400 ± 100 Hz) is identified by INCA as this optimum frequency. The s-m-d model identifies the primary frequency (i.e., 3600 Hz) as this optimum frequency for each noise amplitude level. That is, the optimal frequency is independent of the noise amplitude.

Fig. 17 shows the variation of amplification and mean bow shock speed with noise rms level at the optimum frequency obtained from the CFD and s-m-d. Based on the CFD results the pressure levels within a given cavity increase nearly *proportionally* with inflow noise rms until the strength of pressure oscillations begins to plateau or saturate. That is, amplification stays nearly constant until saturation occurs at a noise rms level of approximately 1-2%. The s-m-d model results indicate that amplification is constant with noise rms. This is expected of the s-m-d model since the input perturbation energy (over one cycle) increases proportionally to noise rms.

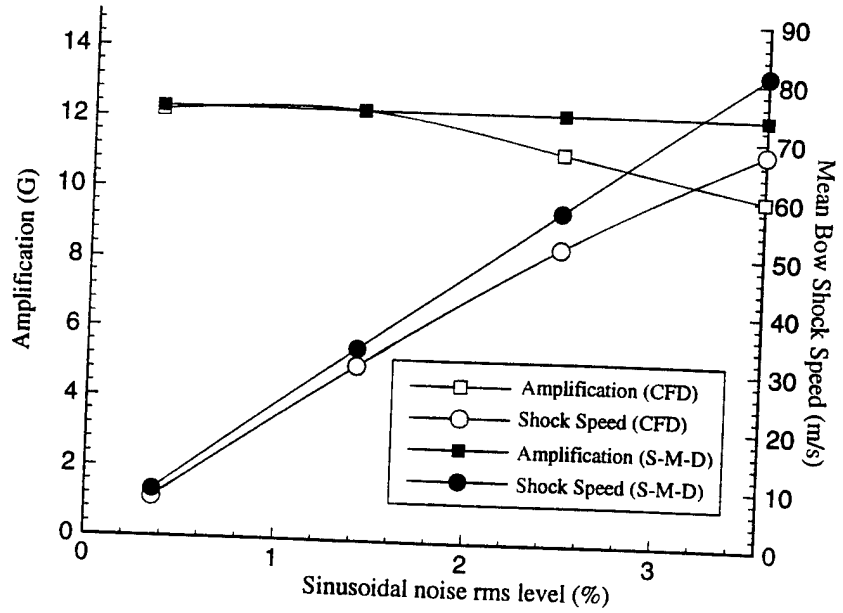

Fig. 17 : Amplification and bow shock speed vs. sinusoidal noise level

These results confirm those of Section 3 in which amplification is shown to be roughly independent of broadband noise amplitude (within a factor of two) based on numerical and experimental data.

The same trend is evident for the variation of mean bow shock speed with noise amplitude (i.e., mean bow shock speed increases proportionally to inflow noise rms). Based on the two illustrated relationships one may deduce that basewall pressure amplitude also increases proportionally to mean bow shock speed (and bow shock oscillation amplitude). This relationship implies a 'stiffness' since as bow shock oscillation amplitude grows so does the basewall pressure amplitude (see also Section 4.1). The s-m-d model results also indicate that mean bow shock speed is proportional to noise rms (and basewall pressure amplitude).

5.3 Sensitivity of Amplification to Noise Variable

Next consider the sensitivity of amplification to the specific choice of noise variable, that is whether the noise is isothermal, isobaric, incompressible, or isentropic. As described earlier, the nominal case includes sinusoidal perturbations in pressure and density (isothermal noise). Fig. 18 illustrates base pressure history (starting from steady flow) for the nominal case at the primary mode frequency (3600 Hz).

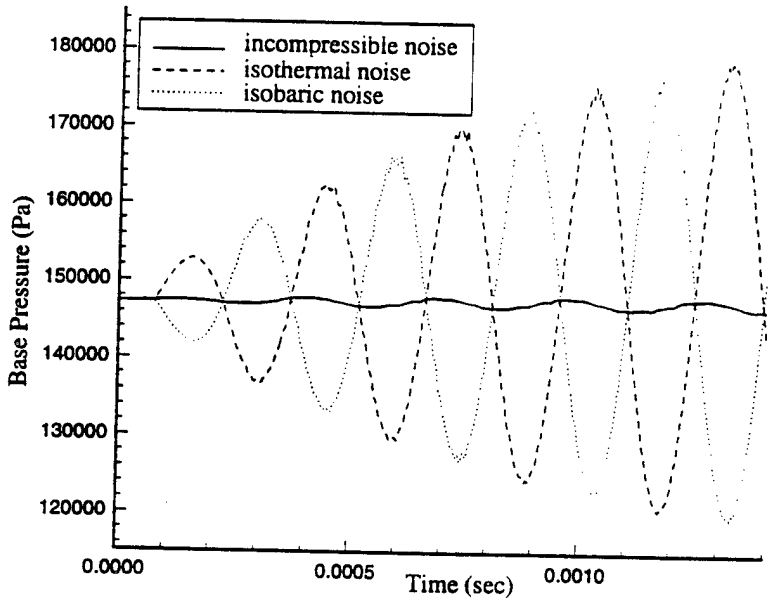

Fig. 18 : Base pressure histories for three noise variable modes (from start-up)

Base pressure histories are also plotted using two other noise models: isobaric (perturbations in temperature and density) and incompressible (perturbations in pressure and temperature). Both the isothermal and isobaric noise models produce the same amplification (but 180° out of phase). Incompressible noise however results in negligible oscillations.

These results may be analyzed using the normal shock relations (and can be similarly demonstrated by the s-m-d model). Suppose the static pressure, density, and temperature, respectively, are defined in terms of the mean values and an arbitrary function of time, *fn(t)*, for isothermal, isobaric, and incompressible noise:

$$\begin{array}{lll} P_1 = \overline{P}\, fn(t) & P_1 = \overline{P} & P_1 = \overline{P}\, fn(t) \\ \rho_1 = \overline{\rho}\, fn(t) & \rho_1 = \overline{\rho}\, fn(t) & \rho_1 = \overline{\rho} \\ T_1 = \overline{T} & T_1 = \overline{T} / fn(t) & T_1 = \overline{T}\, fn(t) \\ \textit{(isothermal)} & \textit{(isobaric)} & \textit{(incompressible)} \end{array} \qquad (25)$$

The pressure ratio across a normal shock as a function of the upstream Mach number (M_1) is given by:

$$\frac{P_2}{P_1} = \frac{2\gamma M_1^{\,2}}{\gamma+1} - \frac{\gamma-1}{\gamma+1} \qquad M_1 = V_1 / \sqrt{\gamma R T_1} \qquad (26)$$

Assuming hypersonic speeds the second term in the pressure jump can be neglected. Substituting the expressions for P_1 from Eqn. 25 and M_1 from Eqn. 26 and rearranging, the final expression for the pressure downstream of the bow shock (P_2) is obtained for each case:

$$\begin{array}{lll} P_2 = \dfrac{2\gamma \overline{M}_1^{\,2}}{\gamma+1} \overline{P}_1 fn(t) & P_2 = \dfrac{2\gamma \overline{M}_1^{\,2}}{\gamma+1} \dfrac{\overline{P}_1}{fn(t)} & P_2 = \dfrac{2\gamma \overline{M}_1^{\,2}}{\gamma+1} \overline{P}_1 \\ \textit{(isothermal)} & \textit{(isobaric)} & \textit{(incompressible)} \end{array} \qquad (27)$$

P_2 is proportional to *fn(t)*, $1/fn(t)$, and 1 for the isothermal, isobaric, and incompressible cases, respectively. Assuming the arbitrary function, *fn(t)*, consists of

a mean value plus small sinusoidal variations (as in the CFD inflow noise model), the amplitudes of $fn(t)$ and $1/fn(t)$ are approximately equal but 180 deg out of phase. The sinusoidal variations in the pressure downstream of the bow shock which drive the oscillations are nearly identical (except out-of-phase) for isothermal and isobaric noise. On the other hand, no variation in the pressure downstream of the bow shock is expected for the incompressible case. Hence, this analysis confirms the CFD results for isothermal, isobaric, and incompressible noise seen in Fig. 18.

Finally, isentropic noise in which static pressure is again defined proportional to the arbitrary time function results in an expression for P_2 shown below. Note that this isentropic noise should be less effective in producing oscillations than isothermal and isobaric noise since $1/\gamma = D. >\ < 1$. CFD results confirm this result by indicating a 25% reduction in amplification for an isentropic noise case.

$$P_2 = \frac{2\gamma \overline{M}_1^{\,2}}{\gamma + 1} \overline{P}_1 (fn(t))^{1/\gamma} \tag{28}$$

5.4 Sensitivity of Amplification to Cavity Geometry

Consider the sensitivity of pressure amplification to cavity geometry. Specifically, sensitivity to cavity depth and cavity lip radius are studied numerically. Typically four separate CFD simulations are performed for each geometry using different frequencies to again isolate the frequency (f_{opt}) which provides the optimum amplification.

Fig. 19 illustrates optimum amplification and mean bow shock speed relative to the body for four sharp lip cavities with different cavity lengths (other geometry features held constant). The CFD results indicate that amplification increases nearly *proportionally* to cavity length over the entire *L/D* range, and that mean bow shock speed increases with cavity length nearly asymptotically. There is remarkably good agreement between CFD and the s-m-d model for both amplification and bow shock speed. The s-m-d model deviates from the CFD the most at L/D=1.25 since the oscillations are strongest and presumably exhibit a more nonlinear acoustic wave behavior.

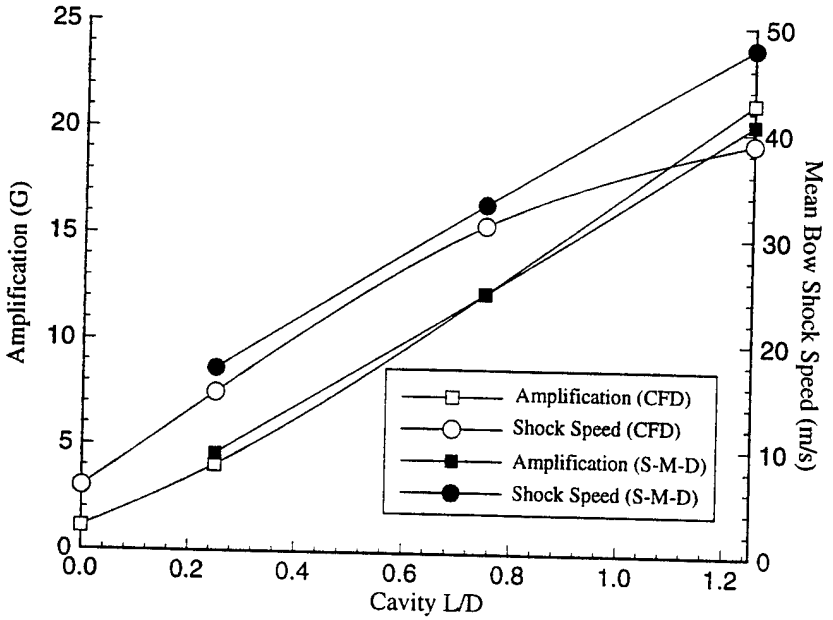

Fig. 19 : Amplification and bow shock speed vs. cavity depth

The perfect agreement for the amplification at L/D=0.75 reflects the fitting of c_1=0.4 at that point.

The effect of geometric scale is studied by comparing the pressure-time history for the nominal L/D=0.75 case at a driving frequency of 3300 Hz with a half-scale version at a driving frequency of 6600 Hz. The resulting pressure-time histories (normalized by frequency) and amplifications (both not shown) are virtually identical indicating dynamic similarity (no sensitivity to scale). This is expected since boundary layers and viscous dissipation forces appear to be quite small. Dynamic similarity, is of course, also preserved in the s-m-d model.

Pressure oscillations are modestly sensitive to lip geometry for the range of lip radii from 0.1 mm to 1.0 mm. Experimental work conducted by Yuceil and Dolling [Ref. 2] at Mach 5 concluded that flow dynamics near the cavity base are not substantially affected by changes in the lip shape. Numerical simulations using a sinusoidal perturbation at Mach 5 indicate weak to modest sensitivity of the amplification parameter to small changes in lip radius. The amplification for L/D=0.25

and L/D=0.75 increase approximately 5% and 25%, respectively, as lip radius is varied between 0.1 mm and 1.0 mm. Note that the optimal frequencies (f_{opt}) for the rounded lip cases were not determined (i.e., f_{opt} was set based on the corresponding sharp lip results). Consequently, the amplification increases may be somewhat larger than indicated. Perhaps the pressure oscillations radiate (lose acoustic energy) more effectively for sharp lip cases since the large separated flow region just outside the cavity mouth, near the lip, represents a stagnation pressure loss (energy loss).

5.5 Sensitivity of Amplification to Nose Diameter

The sensitivity of amplification to body nose diameter is studied in a similar manner to the sensitivity to cavity depth. Again, typically four separate CFD simulations are performed for each geometry using different frequencies to isolate the frequency which provides the optimum amplification. The cavity geometry is fixed (i.e., nominal case, L=1.91 cm, D=2.54 cm, L/D=0.75). The freestream noise model is again ±2% sinusoidal perturbations in pressure and density at Mach 5.

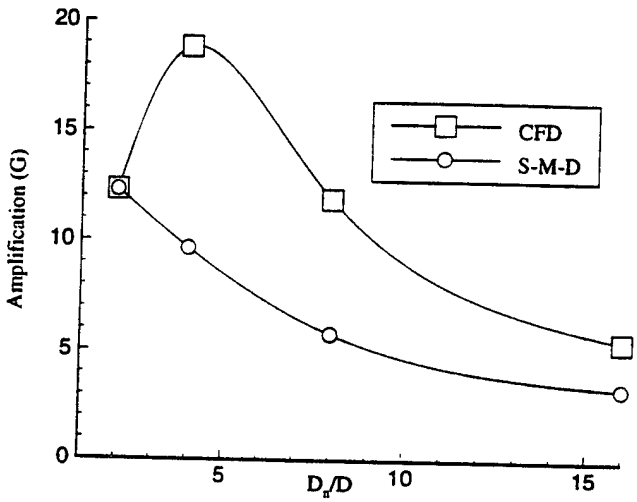

Fig. 20 : Amplification vs. nose diameter
(cavity diameter (D) = 2.54 cm)

Fig. 20 illustrates spline-fitted CFD results for optimum amplification versus nose diameter. These results indicate that peak amplification varies with nose diameter

(D_n) ratio, D_n/D, in a highly non-linear fashion, reaching a maximum quickly (near $D_n/D = 4$) and then gradually decreasing for larger nose diameters. The s-m-d model results show a monotonic decline in amplification with nose diameter. Note that the gradually decreasing trends for both the CFD (for $D_n/D > 4$) and s-m-d results indicate that amplification is almost inversely proportional to D_n. Based on the dissipation mechanism described earlier it is expected that amplification would decrease smoothly as nose diameter increases since as the bow shock is further removed from the body the reflection of acoustic energy is less efficient. However, it is likely that radial spreading of the acoustic waves traveling between the cavity mouth and bow shock is responsible for the more rapid decrease in amplification in the CFD.

One possible explanation for the maximum in the CFD results involves the strong convection currents at the cavity mouth (see Fig. 21a). These currents are quite strong when the bow shock is relatively close to the cavity mouth (e.g., radial velocities of approximately Mach 0.5). These currents weaken quickly as nose diameter is increased since the bow shock moves upstream (see Fig. 21b). Strong convection increases the acoustic wave speeds in the radial direction thereby diffusing the acoustic energy traveling between the bow shock and cavity mouth and reducing the acoustic efficiency of the system. Hence, small nose diameter bodies could be expected to produce higher dissipation and lower amplification. Note that the 1-D s-m-d model assumes no radial spreading of waves and cannot emulate these results.

The optimum frequency from the CFD simulations essentially does not change as nose diameter increases, even though the characteristic frequency (Eqn. 2) decreases as the standoff distance decreases. When the shock standoff distance is relatively large the cavity gas approaches a quasi-static condition (Section 4) at the primary frequency (i.e., cavity dimensions are small compared to the oscillation length scale). The cavity flow is able to equilibrate relatively quickly compared to the oscillation time scale ($\sim$ set by δ) and it becomes difficult to achieve a strong pressure gradient within the cavity during the oscillation. Consequently, it is reasonable to expect that the optimum frequency for large D_n/D cases would be closer to that posed by the cavity depth (L) as the characteristic length scale rather than L^*.

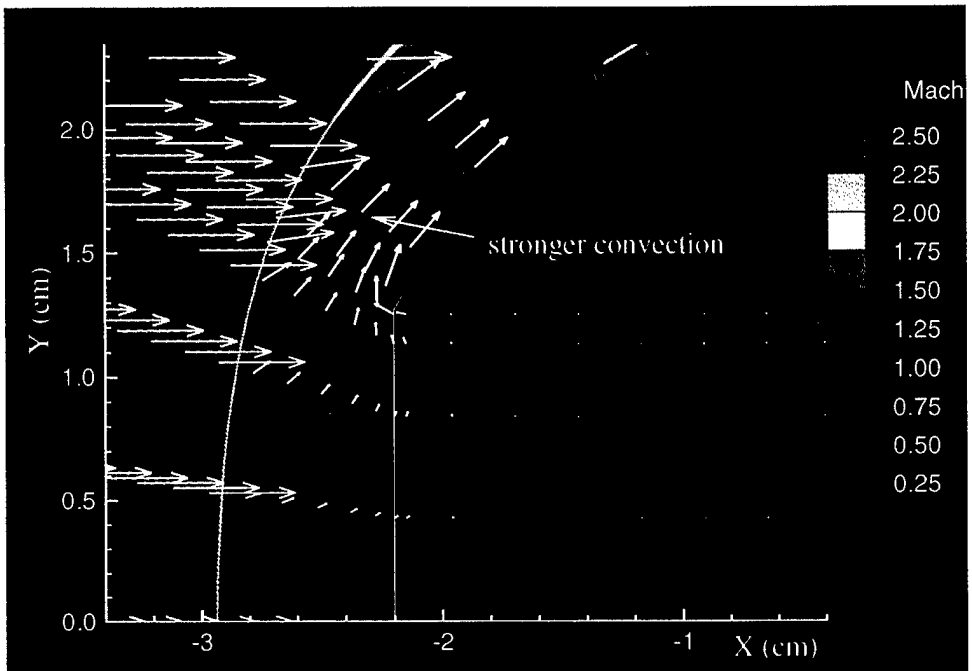

Fig. 21a : Steady flow mach number contours ($D_n/D = 2$)

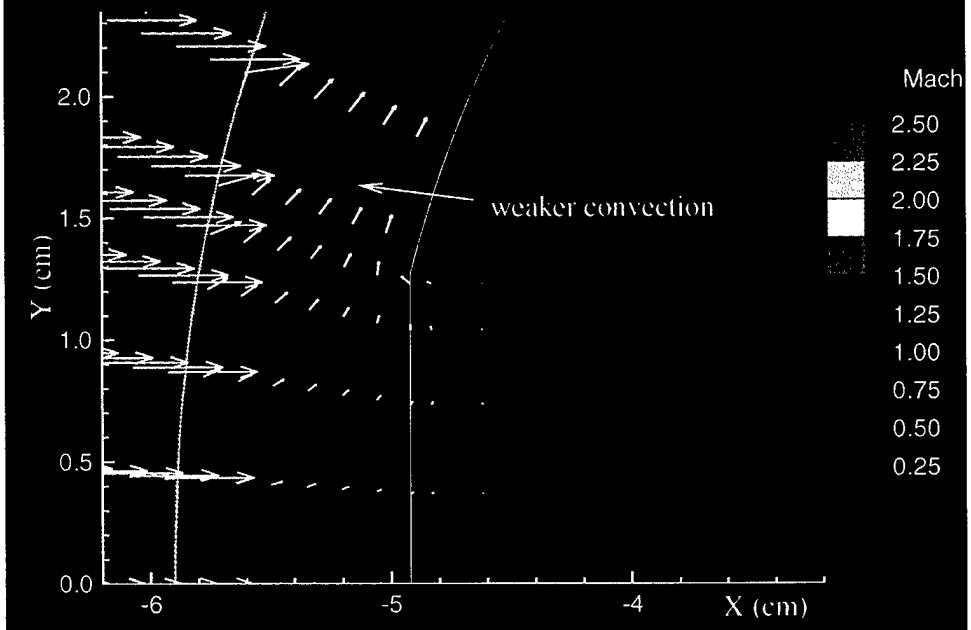

Fig. 21b : Steady flow mach number contours ($D_n/D = 4$)

5.6 Sensitivity of Amplification to Mach Number

Consider next the effect of Mach number on pressure amplification. Numerical simulations are performed using the geometrically nominal L/D=0.75 case but at different Mach numbers. In each simulation adiabatic wall conditions are implemented and the flow is assumed calorically perfect. Typically four separate simulations are performed for each Mach number using different frequencies to isolate the frequency which provides the optimum amplification.

Fig. 22 shows the variation of amplification with input frequency for Mach 2, 3, 5, 7, and 9. CFD results indicate that amplification increases rapidly with Mach number for low Mach numbers but begins to level-off at hypersonic speeds. S-m-d results also demonstrate that amplification levels-off with Mach number. However, the two asymptotes are moderately different in slope and in final asymptotic value. The s-m-d model produces this asymptotic trend because the dissipation is directly proportional to the steady flow bow shock stand-off distance which asymptotically decreases with Mach number.

5.7 Sensitivity of Amplification to Viscous Effects

The effect of fluid viscosity was studied by comparing the base pressure history for the nominal L/D=0.75 case with the same case but including an inviscid fluid constraint (i.e., viscosity = 0). The inviscid solution was virtually identical (not shown) to the nominal viscous solution indicating that the mechanisms of resonance and dissipation are inviscid phenomena. This is unlike a Helmholtz resonator near a reflector for which viscous dissipation is the primary dissipation mechanism [Ref. 11].

5.8 Sensitivity of Amplification to Thermal Constraint

CFD results indicate that the thermal wall constraint (i.e., isothermal wall vs. adiabatic wall) has a weak effect on amplification for cases which involve a small temperature potential (i.e., the wall temperature is close to the stagnation temperature). For example, the nominal L/D=0.75 case with an isothermal wall at 300 K shows a reduction in the amplification of less than 2% if an adiabatic wall is used instead.

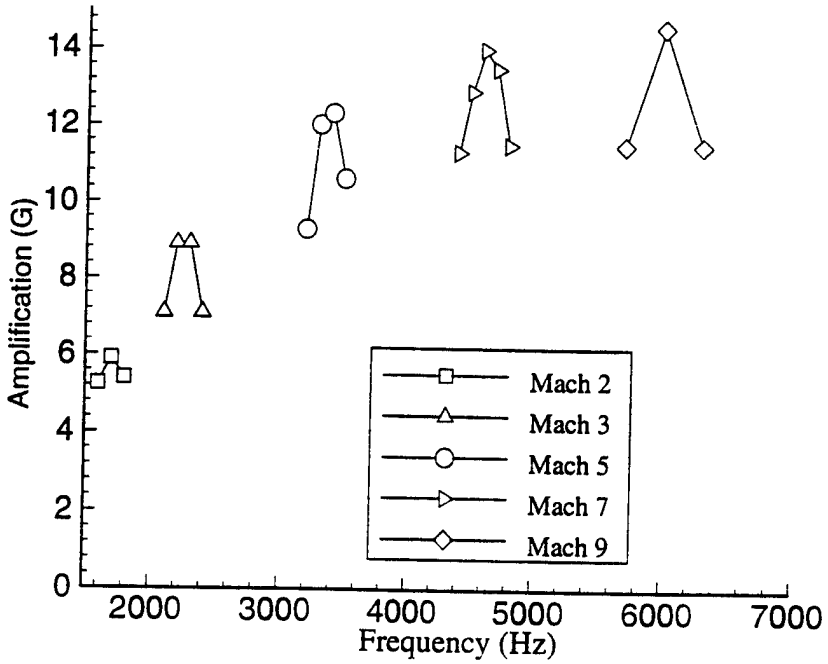

Fig. 22a : Peak amplification vs. mach number (CFD)

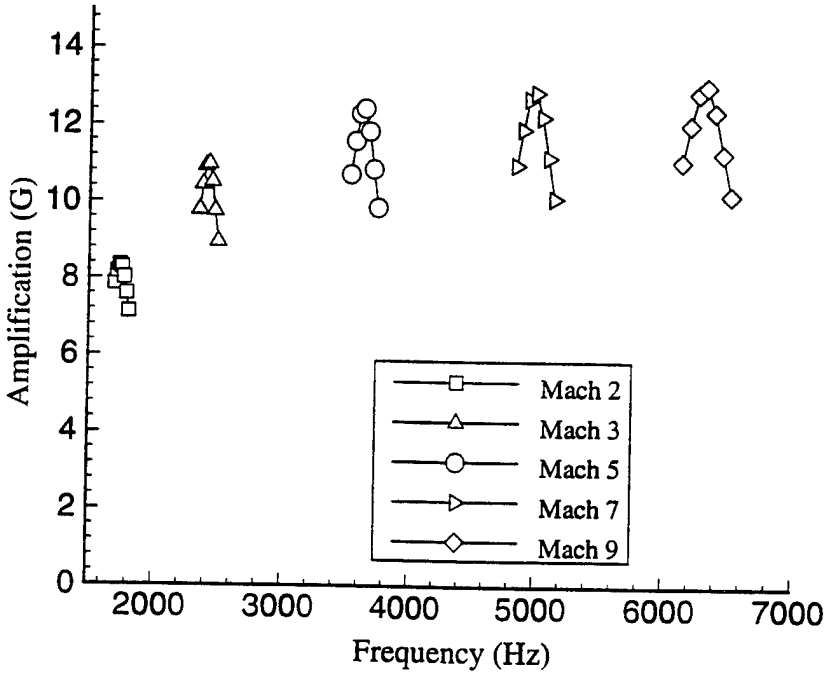

Fig. 22b : Peak amplification vs. mach number (S-M-D)

However, if the temperature potential is large then amplification is significantly reduced. Simulation results for the nominal geometric configuration at Mach 9 with isothermal wall (300 K) and adiabatic wall conditions showed a moderate reduction (i.e., 30%) in amplification in the isothermal wall case. Perhaps the large radial temperature gradients within the cavity cause the resonant frequency to become a strong function of radial position and this ambiguity leads to significantly reduced amplification.

6 S-M-D Model Response to Broadband Noise

In order to further study and verify the s-m-d model described in Section 4 another set of comparisons to CFD results are conducted in which the response of the s-m-d model to broadband noise for various cavity depths ($L/D \leq 1.25$) at Mach 5 is compared to the appropriate CFD results from Section 3. The s-m-d model is exactly the same as implemented in Section 5 except the variation of freestream static pressure with time is the same as implemented in the related CFD Mach 5 simulations.

Fig. 23 shows the variation of amplification with cavity depth at Mach 5 obtained from the CFD and the s-m-d model.

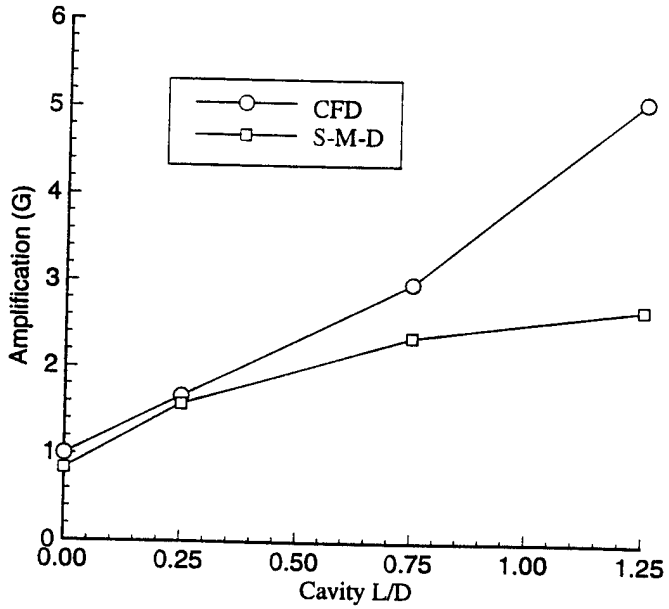

Fig. 23 : Cavity response to broadband noise

The s-m-d model predicts somewhat low values but follows the basic trend (i.e., increasing with depth) for a while. Recall that CFD and s-m-d model results for amplification vs. frequency (Fig. 12) indicate that the peaks amplifications are similar but broadened in the CFD results. Assuming the effect of noise energy at each individual frequency may be summed, it is reasonable to expect that the CFD would produce the larger amplification in response to 'white' noise. In deeper cavities (Fig. 15) the difference in sharpness of the amplification peaks between the CFD and s-m-d becomes more dramatic which might explain why the amplification curves diverge in Fig. 23.

7 Self-Sustaining Mechanism

As mentioned earlier it would appear quite difficult to model the fluid dynamics of self-sustaining cases (i.e., relatively deep cavities) which exhibit strong, non-sinusoidal shock motion and nonlinear acoustic wave behavior. The relative motion of the bow shock can no longer be ignored in the model. In fact, two arguments are presented below that the motion of the shock is directly related to the self-sustaining phenomenon.

Consider a bow shock oscillating in front of a typical nose-cavity. Analytically it may be shown that momentum losses across a bow shock (i.e., internal viscous dissipation or loss of stagnation pressure) increase with forward shock motion and decrease with aft shock motion. Consequently, it would appear that inflow momentum (i.e., the driving force) is larger during cavity inflow than during cavity outflow. During cavity inflow the freestream flow momentum tends to reinforce the cavity flow since both flow in the same direction (i.e., cavity flow is energized). During cavity outflow the freestream momentum opposes the cavity flow (i.e., cavity flow energy is depleted). Thus, due to the relative imbalance in losses across the moving shock even symmetric (e.g., sinusoidal) bow shock oscillations might tend to add energy to the cavity fluid oscillations. This energy addition would increase with mean bow shock speed, perhaps acting like a 'reverse dissipation'.

From another point of view and based on fluid dynamic animations, it appears that the flow field is fundamentally different during cavity inflow and outflow phases.

During cavity inflow (Fig. 8a) there is relatively low pressure and high velocity downstream of the bow shock and the incoming airstream flows directly into the cavity without significant radial flow (i.e., the axisymmetric 'relieving' effect is small). In contrast, during cavity outflow (Fig. 8b) there is relatively high pressure and low velocity downstream of the bow shock and the incoming airstream tends to flow radially around the blunt nose. Consequently, it would appear that the 'relieving' effect is strongest during cavity outflow, reducing or deflecting the momentum of the incoming stream. Again, bow shock motion appears to be creating a 'reverse dissipation' since the effect should grow with mean bow shock speed.

If this 'reverse dissipation' exists, a self-sustaining phenomenon could occur for certain nose-cavity configurations which produce a relatively small amount of radiation resistance (b). Recall, radiation resistance decreases monotonically with cavity depth according to Eqn. 18. Similarly, the damping ratio decreases monotonically with cavity depth according to recent experimental work at Mach 4 [Ref. 15]. Suppose the 'reverse dissipation' remains constant with cavity depth. It follows that as cavity depth increases eventually the total dissipation would change sign (i.e., become negative) and the flow would resonate strongly without freestream noise. This likely accounts for the rapid change in amplification with L/D in Figs. 4a and 4b. Other damping mechanisms (e.g., those associated with strong oscillations) would presumably keep the oscillations from becoming unbounded.

Preliminary time-accurate CFD simulation results involving different 2-D (non-axisymmetric) cavity geometries and freestream Mach numbers (not discussed herein) indicate that 2-D forward-facing cavities in hypersonic flows do *not* self-sustain resonant oscillations. However, these 2-D nose-cavity geometries do amplify sinusoidal inflow noise perturbations similar to the axisymmetric cases. These trends imply that the self-sustaining mechanism is related to the relatively strong relieving effect present in axisymmetric cases (perhaps in the manner described above) and that the noise-driven mechanism is primarily a 1-D phenomenon (as suggested by the s-m-d model).

8 Summary

The agreement shown between computations and experiments implies that freestream noise in a small bandwidth of frequencies near the primary mode is the mechanism which drives resonant pressure oscillations within relatively shallow forward-facing cavities. On the other hand, numerical simulations indicate that relatively deep cavities are unstable and will oscillate without freestream noise (i.e., self-sustain resonant oscillations).

The response of relatively shallow cavities to inflow noise is somewhat analogous to a damped harmonic oscillator. A spring-mass-damper (s-m-d) model was developed based on analytical study and fluid dynamic observations. The cavity fluid accelerates almost uniformly, like an oscillating piston, and is approximated by a rigid mass element. These flows also exhibit a 'stiffness' since the basewall pressure amplitude increases almost proportionally to bow shock amplitude. Dissipation arises from baffled-piston-like radiation losses. The bow shock acts as a reflector placed and ahead of the piston.

A parametric study of relatively shallow cavities established the sensitivity of amplification (gain) to noise frequency, noise amplitude, noise variable type, cavity depth, cavity lip radius, body nose diameter, geometric scale, Mach number, viscous and thermal wall conditions. Reasonable agreement between the CFD and s-m-d model was obtained for most of these parameters.

Acknowledgment

This work was supported by the U.S. Army Research Laboratory (ARL) under contract DAAA21-93-C-0101.

References

1. Yuceil, B., Dolling, D. S., and Wilson, D. E., "A Preliminary Investigation of the Helmholtz Resonator Concept for Heat Flux Reduction," AIAA Paper 93-2742, July 1993.

2. Yuceil, B., and Dolling, D.S., "Effects of a Nose Cavity on Heat Transfer and Flowfield Over a Blunt Body at Mach 5," AIAA Paper 94-2050, Jun. 1994.

3. Engblom, W.A., Yuceil, B., Goldstein, D.B., and Dolling, D.S., "Experimental and Numerical Study of Hypersonic Forward-Facing Cavity Flow," *AIAA Journal of Spacecraft and Rockets*, Vol. 33, No. 3, pp. 353-359, 1996.

4. Engblom, W.A., Goldstein, D.B., Ladoon, D., and Schneider, S., "Fluid Dynamics of Forward-Facing Cavity Flow," AIAA Paper 96-0667, Jan. 1996.

5. Engblom, W.A., Goldstein, D.B., "Nose-Tip Surface Heat Reduction Mechanism," AIAA Paper 96-0354, Jan. 1996. (and to appear in the *AIAA Journal of Thermophysics and Heat Transfer*)

6. Engblom, W.A., Numerical Investigation of Hypersonic Flow Over a Forward-Facing Cavity, University of Texas at Austin, PhD Dissertation, Aug. 1996.

7. Yuceil, B., An Experimental Investigation of a Forward-Facing Nose Cavity on a Blunt Body at Mach 5, University of Texas at Austin, PhD Dissertation, Dec. 1995, pp. 77-94, 123-132.

8. Yuceil, B., and Dolling, D.S., "IR Imaging and Shock Visualization of Flow over a Blunt Body with a Nose Cavity," AIAA Paper 96-0232, Jan. 1996.

9. Huebner, L.D., and Utreja, L.R., "Mach 10 Bow-Shock Behavior of a Forward-Facing Nose Cavity," *J. of Spacecraft and Rockets*, Vol. 30, No. 3, May-June 1993.

10. Blackstock, D.T., Introduction to Physical Acoustics, draft textbook, The University of Texas at Austin, 1995, Chapters 4, 13.

11. Morse, P.M. and Ingard, U., Theoretical Acoustics, Princeton Univ. Press, Princeton, NJ, 1986, pp. 482-483.

12. Wilson, D.E., Private Communication, University of Texas at Austin, Professor, Mechanical Engineering Dept., June 1996.

13. Swift, G.W., "Thermoacoustic Engines and Refrigerators," Physics Today, July 1995.

14. Powell, A., and Smith, T.J., "Experiments Concerning the Hatrmann Whistle," Report 64-42, UCLA Dept. of Engineering, Sep. 1964.

15. Ladoon, D., and Schneider, S.P., "Laser-Induced Resonance in a Forward-Facing Cavity at Mach 4," AIAA draft paper, submitted to 35th AIAA Aerospace Sciences Meeting and Exhibit, Reno, Jan. 1997.

16. Anderson, J.D., Hypersonic and High Temperature Gas Dynamics, McGraw-Hill, 1989, p. 189.

Distribution List

Administrator
Defense Technical Information Center
Attn: DTIC-DDA
8725 John J. Kingman Road, Ste 0944
Ft. Belvoir, VA 22060-6218

Director
US Army Research Lab
ATTN: AMSRL OP SD TA
2800 Powder Mill Road
Adelphi, MD 20783-1145

Director
US Army Research Lab
ATTN: AMSRL OP SD TL
2800 Powder Mill Road
Adelphi, MD 20783-1145

Director
US Army Research Lab
ATTN: AMSRL OP SD TP
2800 Powder Mill Road
Adelphi, MD 20783-1145

Army Research Laboratory
AMSRL-CI-LP
Technical Library 305
Aberdeen Prvg Grd, MD 21005-5066

William deRosset
U.S. Army Research Laboratory
Attn: AMSRL-WT-TC
Aberdeen Prvg Grd, MD 21005-5066

Tom Doligalski
US Army Research Office
P. O. Box 12211
Research Triangle Park, NC
27709-2211

Dr. Hartmut H. Legner
Principal Research Scientist
Physical Sciences Inc.
20 New England Business Ctr.
Andover, MA 01810-1022

P. Plostins
Director
US Army Research Lab
Aberdeen Prvg Grd, MD 21005-5066

Edward Schmidt
U.S. Army Research Laboratory
Attn: AMSRL-WT-PB
Aberdeen Prvg Grd, MD 21005-5066

David J. Scott
Head of W6 Division
DRA Military Divison
Fort Halstead Sevenoaks
WG Division
Kent, TN14 7BY
United Kingdom

Dr. George D. Waldman
Consultant
511 West Street
Reading, MA 01867

P. Weinacht
Director
US Army Research Lab
Aberdeen Prvg Grd, MD 21005-5066